



# Weak persistence of Northwest Pacific anomalous anticyclone during post-El Niño summers in CMIP5 and CMIP6 models

Haosu Tang<sup>1,2,5</sup> · Gang Huang<sup>1,2,5</sup> · Kaiming Hu<sup>1,4</sup> · Wenping Jiang<sup>3</sup> · Weichen Tao<sup>1</sup> · Ya Wang<sup>1</sup> · Hongyu Hou<sup>1,5</sup>

Received: 3 November 2022 / Accepted: 29 March 2023 / Published online: 10 April 2023  
© The Author(s), under exclusive licence to Springer-Verlag GmbH Germany, part of Springer Nature 2023

## Abstract

An anomalous anticyclone (AAC) recurs over the Indo-Northwest Pacific during post-El Niño summers, regulating climate anomalies in the densely populated South, Southeast, and East Asia. However, AACs simulated in phase 5/6 of the Coupled Model Intercomparison Project (CMIP5/6) multi-model ensemble mean fail to persist through post-El Niño summers. The present study suggests that this weak persistence bias likely stems from the weakly persistent sea surface temperature (SST) anomalies' gradient between the North Indian Ocean and tropical Western Pacific. On one hand, the simulated North Indian Ocean warming decays faster compared with its observational counterpart due to the weakened cross-equatorial antisymmetric wind patterns and wind–evaporation–SST feedback, which may arise from the deep thermocline bias in the Southwest Indian Ocean in CMIP models. On the other hand, the long-lasting Western Pacific warming bias may be led by the intensified upper-ocean zonal advection feedback and wind–downwelling–SST feedback, which can be further traced back to the Pacific cold tongue bias in CMIP models. Compared with CMIP5 models, CMIP6 models simulate a more realistic Southwest Indian Ocean thermocline dome and equatorial Pacific cold tongue. Therefore, the overall simulation skill in the summertime AAC persistence is improved in CMIP6 than in CMIP5 models. The persistence of AAC is further investigated during post-Eastern Pacific (EP) and Central Pacific (CP) El Niño summers in CMIP models. The simulated AAC displays a remarkable stronger persistence during post-EP El Niño summer compared to its post-CP counterpart. The present study highlights that reducing mean-state biases in climate models may elevate the simulation skills of summertime AAC persistence, thereby enhancing seasonal prediction and future projection skills of Asian summer monsoon.

**Keywords** El Niño · Anomalous anticyclone · Persistence · Thermocline · Cold tongue bias

✉ Gang Huang  
hg@mail.iap.ac.cn

✉ Kaiming Hu  
hkm@mail.iap.ac.cn

<sup>1</sup> State Key Laboratory of Numerical Modeling for Atmospheric Sciences and Geophysical Fluid Dynamics (LASG)/Center for Monsoon System Research (CMSR), Institute of Atmospheric Physics, Chinese Academy of Sciences, Beijing, China

<sup>2</sup> Laboratory for Regional Oceanography and Numerical Modeling, Qingdao National Laboratory for Marine Science and Technology, Qingdao, China

<sup>3</sup> Key Laboratory of Marine Hazards Forecasting, Ministry of Natural Resources/College of Oceanography, Hohai University, Nanjing, China

<sup>4</sup> Collaborative Innovation Center on Forecast and Evaluation of Meteorological Disasters (CIC-FEMD), Nanjing University of Information Science and Technology, Nanjing, China

<sup>5</sup> University of Chinese Academy of Sciences, Beijing, China

## 1 Introduction

El Niño–Southern Oscillation (ENSO), originating from equatorial central and eastern Pacific, is the dominant mode of climate fluctuation at interannual timescale and exerts far-reaching impacts across the world (e.g., McPhaden et al. 2006; Hu et al. 2021). ENSO is generally phase locked to an annual cycle, which features growth in boreal summer, mature during winter, and fade in the following spring (hereafter seasons denote those of the Northern Hemisphere). A low-level anomalous anticyclone (AAC) anchored to the Indo-Northwest Pacific (NWP) is a recurrent pattern during post-El Niño summers, bridging preceding El Niño with Asian summer monsoon and posing extensive climate impacts on the densely populated South, Southeast, and East Asia (EA). Specifically, the AAC could transport water vapor from tropical oceans to EA and Indian peninsula through southwesterly winds along its western periphery,

inducing heavy rainfall even severe floods via intensifying low-level moisture convergence (Chang et al. 2000; Chowdary et al. 2013; Tang et al. 2022a, b). Meanwhile, the areas cloaked in the ridge of the AAC often suffer from sunny and scorching weathers mainly due to enhanced adiabatic subsidence heating and solar radiation (Hu et al. 2011; Deng et al. 2019). Moreover, the AAC could break the summer NWP monsoon trough, thereby suppressing local tropical cyclone genesis (Du et al. 2011). The AAC is generally considered as the tropical lobe of the Pacific–Japan/East Asia-Pacific (PJ/EAP) teleconnection pattern (Nitta 1987; Huang and Sun 1992). Together with the anomalous cyclonic circulation to its northeast, the AAC spanning the Indo–NWP warm pool can further influence the synoptic weather and climate in the mid-latitude of EA and serve as the principal origin of seasonal predictability for EA summer climate (Kosaka et al. 2013).

As for the formation and maintenance mechanisms of AAC pattern, the El Niño-induced cold sea surface temperature anomalies (SSTA) over tropical NWP can suppress local convective activities and excite a low-level AAC as the atmospheric Rossby wave response on its northwest side. The AAC further reinforces the NWP cold SSTA via the wind–evaporation–SST (WES) feedback, persisting into El Niño decaying summer (Wang et al. 2000; Li et al. 2017). Nevertheless, the tropical NWP cold SSTA gradually decline with the withdrawal of the northeasterly trade winds during El Niño decaying summer. Therefore, another school of studies indicated that the El Niño-induced Indian Ocean basin (IOB) warming can serve as a capacitor in maintaining the summer AAC pattern via the Kelvin wave-induced surface Ekman divergence mechanism (Xie et al. 2009). These two schools of opinions further evolved into the Indo–western Pacific Ocean capacitor effect, which highlights the roles of both IO and tropical NWP (Kosaka et al. 2013; Xie et al. 2016; Du et al. 2022).

Summer (June to August) is the monsoon season for EA when the rainfall variability exerts immense socioeconomic impacts. Previous studies concerning EA summer rainfall variability mainly focused on the seasonal mean climate diagnosis and assessment. However, summer climate in EA experiences dramatic variations on the sub-seasonal timescale (Ye and Lu 2010; Xiang et al. 2013; Li et al. 2022). For example, summer rain belt in EA is not stagnant but shifts northward gradually, accompanied by the northward jump of western Pacific subtropical high (WPSH) (Tao and Chen 1987). These sub-seasonal changes of background mean-states over EA–NWP can further lead to the intensification and northward extension of AAC in post-El Niño mid-summer, whereas the northward shift phase of AAC lags that of background mean-state WPSH (Tang et al. 2021). As a result, the decaying El Niño usually hinders the summer northward jump of WPSH and the concomitant rain belt over

EA, exposing the Yangtze River basin to an elongated wet season with diminished sunlight.

Coupled general circulation models (CGCMs) are essential tools in seasonal prediction and future projection. Given the impacts of AAC on weather and climate anomalies across the Indo–EA, it requires an in-depth assessment of how well the AAC pattern is simulated in the state-of-the-art CGCMs archived in the Coupled Model Intercomparison Project (CMIP). Most CGCMs can capture the general characteristics (i.e., spatial and seasonal features) of the AAC and show relatively high skills in simulating and predicting AAC-related precipitation and temperature anomalies during post-El Niño summers (Chowdary et al. 2010; Kim et al. 2012). Nonetheless, systematic biases (deviations from observations) exist in the detailed properties of the simulated summer AAC. Previous studies indicated that CMIP models suffer from a common underestimation of AAC magnitude during post-El Niño summers. As regards the origins, several studies suggested that the weakened IO capacitor effect and excessive westward extension of El Niño-related SSTA should take responsibility for the weak magnitude bias of the simulated AAC (Tao et al. 2016, 2018, 2019; Jiang et al. 2017; Li et al. 2019).

Previous studies have identified different flavors of El Niño, of which the most widely accepted classification is the Eastern Pacific (EP) and Central Pacific (CP) El Niño (Ashok et al. 2007; Yu and Kim 2013). The maximum SSTA of EP and CP El Niño normally take place in the eastern and central equatorial Pacific, respectively, posing distinct impacts on the weather and climate across the world (Yu et al. 2012). Several studies have indicated that the AAC may respond diversely to two types of El Niño (Chen and Li 2021; Wang et al. 2021). The AAC and its accompanying climate anomalies are generally weaker during post-CP El Niño summers than those during post-EP El Niño summers (Feng et al. 2011; Yuan and Yang 2012; Jiang and Li 2022). Recent studies have examined the performance of ENSO diversity and the associated atmospheric teleconnections and climate phenomena under EP and CP El Niño in CMIP5/6 models (Zou et al. 2014; Xu et al. 2017; Freund et al. 2020). The amplitude and structure of CP El Niño are found better simulated in CMIP6 MME compared with CMIP5 MME (Hou and Tang 2022), possibly attributed to the reduced mean-state SST bias in the Niño-4 region (Jiang et al. 2021).

Compared with the seasonal mean magnitude of summertime AAC, its sub-seasonal evolution in CMIP models is less evaluated but of vital realistic significance (Yu et al. 2021). Pioneering studies have implied a poor persistence of AAC during post-El Niño summers in CMIP5 models (Du et al. 2013; Hu et al. 2014). However, the underlying physical mechanisms are not yet adequately clarified and remain a knowledge gap. Therefore, the present study aims to systematically investigate the persistence of summertime AAC

**Table 1** Details of 45 CMIP6 and 36 CMIP5 models used in the present study

CMIP6 (45)	Atmos. resolution (lat × lon)	CMIP5 (36)	Atmos. resolution (lat × lon)	Institute
ACCESS-CM2	1.25° × 1.875°	ACCESS1-0	1.24° × 1.875°	CSIRO–BOM/Australia
ACCESS-ESM1-5	1.24° × 1.875°	ACCESS1-3	1.24° × 1.875°	
BCC-CSM2-MR	1.125° × 1.125°	bcc-csm1-1-m	1.125° × 1.125°	BCC-CMA/China
BCC-ESM1	2.81° × 2.81°	bcc-csm1-1	2.81° × 2.81°	
/	/	BNU-ESM	2.81° × 2.81°	BNU/China
CAMS-CSM1-0	1.125° × 1.125°	/	/	CAMS/China
CanESM5-CanOE	2.81° × 2.81°	/	/	CCCma/Canada
CanESM5	2.81° × 2.81°	CanESM2	2.81° × 2.81°	
CESM2-FV2*	1.875° × 2.5°	CESM1-BGC	0.94° × 1.25°	NSF-DOE-NCAR/United States
CESM2-WACCM-FV2*	1.875° × 2.5°	CESM1-CAM5	0.94° × 1.25°	
CESM2-WACCM	0.94° × 1.25°	CESM1-WACCM*	1.875° × 2.5°	
CESM2*	0.94° × 1.25°	CCSM4	0.94° × 1.25°	
/	/	CESM1-FASTCHEM	0.94° × 1.25°	
/	/	CMCC-CESM	3.75° × 3.75°	CMCC/Italy
/	/	CMCC-CMS	1.875° × 1.875°	
/	/	CMCC-CM	0.75° × 0.75°	
CNRM-CM6-1-HR	0.5° × 0.5°	/	/	CNRM-CERFACS/France
CNRM-CM6-1	1.4° × 1.4°	CNRM-CM5	1.4° × 1.4°	
CNRM-ESM2-1	1.4° × 1.4°	/	/	
/	/	CSIRO-Mk3-6-0	1.875° × 1.875°	CSIRO/Australia
E3SM-1-0	1° × 1°	/	/	E3SM-Project/United States
E3SM-1-1-ECA*	1° × 1°	/	/	
E3SM-1-1*	1° × 1°	/	/	
EC-Earth3-Veg	0.7° × 0.7°	/	/	
EC-Earth3	0.7° × 0.7°	/	/	
FGOALS-f3-L	1° × 1.25°	FGOALS-s2	1.67° × 2.81°	LASG-CES/China
FGOALS-g3	2.25° × 2°	FGOALS-g2	3° × 2.81°	
/	/	FIO-ESM	2.81° × 2.81°	FIO/China
GFDL-CM4	1° × 1.25°	GFDL-CM3*	2° × 2.5°	NOAA-GFDL/United States
GFDL-ESM4	1° × 1.25°	GFDL-ESM2G	2° × 2.5°	
/	/	GFDL-ESM2M	2° × 2.5°	
GISS-E2-1-G-CC	2° × 2.5°	/	/	NASA-GISS/United States
GISS-E2-1-G	2° × 2.5°	GISS-E2-R	2° × 2.5°	
GISS-E2-1-H*	2° × 2.5°	GISS-E2-H	2° × 2.5°	
HadGEM3-GC31-LL	1.25° × 1.875°	/	/	MOHC/United Kingdom
HadGEM3-GC31-MM	0.56° × 0.83°	/	/	
INM-CM4-8	1.5° × 2°	inmcm4	1.5° × 2°	INM/Russia
INM-CM5-0	1.5° × 2°	/	/	
IPSL-CM6A-LR	1.26° × 2.5°	IPSL-CM5A-LR	1.875° × 3.75°	IPSL/France
/	/	IPSL-CM5A-MR	1.26° × 2.5°	
/	/	IPSL-CM5B-LR	1.875° × 3.75°	
KACE-1-0-G*	1.25° × 1.875°	/	/	NIMS-KMA/Korea
MCM-UA-1-0	2.25° × 3.75°	/	/	UA/United States
MIROC-ES2L*	2.81° × 2.81°	MIROC-ESM	2.81° × 2.81°	MIROC/Japan
/	/	MIROC-ESM-CHEM	2.81° × 2.81°	
MIROC6	1.4° × 1.4°	MIROC5	1.4° × 1.4°	
MPI-ESM-1-2-HAM	1.875° × 1.875°	/	/	DKRZ/German
MPI-ESM1-2-HR	0.94° × 0.94°	MPI-ESM-MR	1.875° × 1.875°	
MPI-ESM1-2-LR	1.875° × 1.875°	MPI-ESM-LR	1.875° × 1.875°	

**Table 1** (continued)

CMIP6 (45)	Atmos. resolution (lat × lon)	CMIP5 (36)	Atmos. resolution (lat × lon)	Institute
MRI-ESM2-0	1.125° × 1.125°	MRI-CGCM3	1.125° × 1.125°	MRI/Japan
NESM3	1.875° × 1.875°	/	/	NUIST/China
NorCPM1	1.875° × 2.5°	NorESM1-M	1.875° × 2.5°	NCC-NMI/Norway
NorESM2-LM	1.875° × 2.5°	NorESM1-ME*	1.875° × 2.5°	
NorESM2-MM	0.94° × 1.25°	/	/	
SAM0-UNICON	0.94° × 1.25°	/	/	SUU/Korea
UKESM1-0-LL	1.25° × 1.875°	/	/	MOHC/United Kingdom

The high-skill models are highlighted by an asterisk

and its physical origins in CMIP models at sub-seasonal timescale. Besides, from CMIP5 to CMIP6, CGCMs have become more skillful in reproducing background mean-state conditions over Indo–NWP and capturing sophisticated multiscale interactions inherent in EA monsoon systems (Jiang

et al. 2022; Yang and Huang 2022). Thus, we also attempt to probe whether CMIP6 models outperform their CMIP5 counterparts in simulating the persistence of summer AAC, and if so, which physical processes contribute to this performance improvement. Furthermore, the present study will

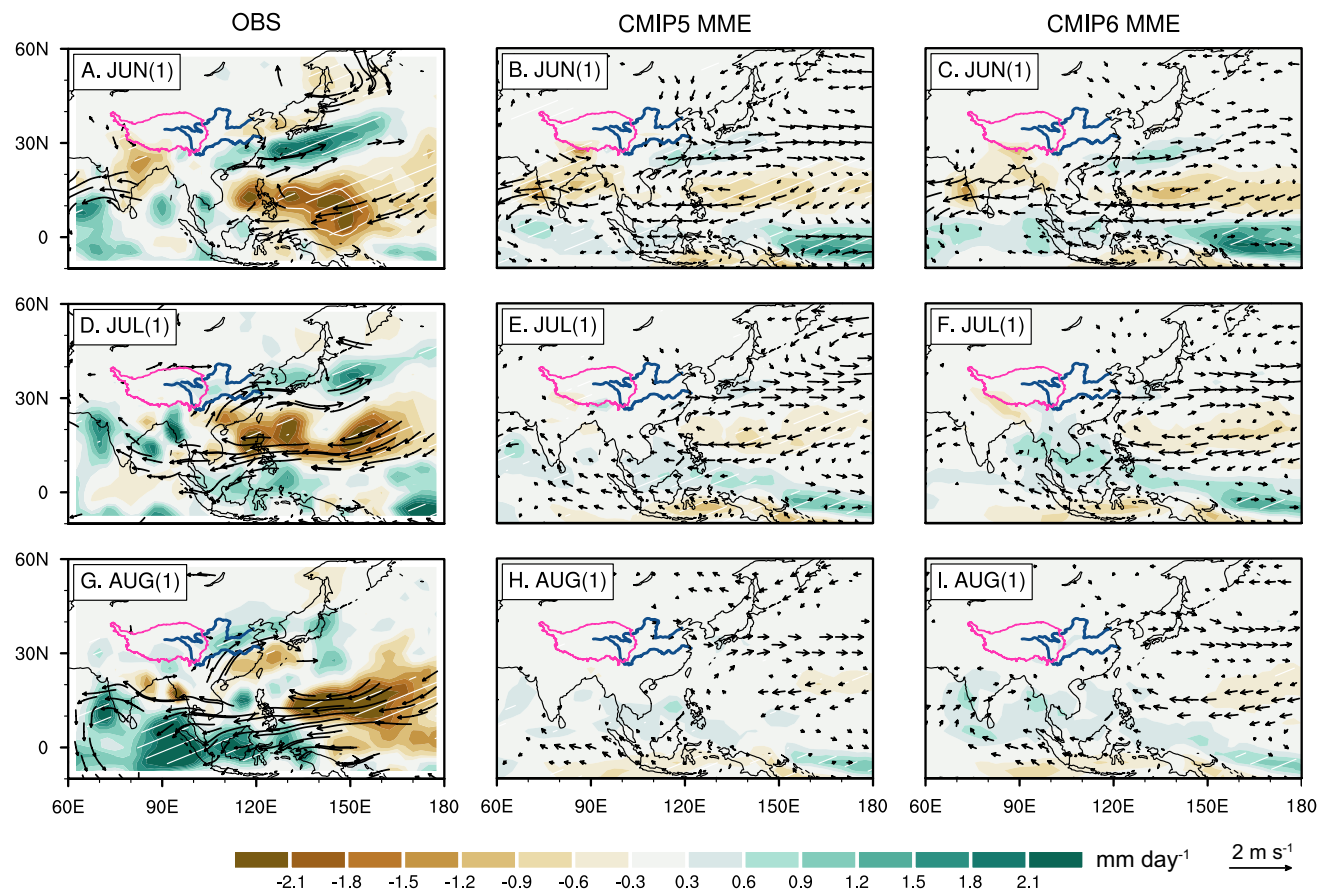


**Fig. 1** 850-hPa wind (vectors; units:  $\text{m s}^{-1}$ ) and precipitation (colors; units:  $\text{mm day}^{-1}$ ) anomalies for the El Niño composite in the observations (left panels), CMIP5 MME (middle panels), and CMIP6 MME (right panels) in June(1) (A–C), July(1) (D–F), and August(1) (G–I). The Tibetan Plateau is highlighted in pink curve and has been masked

out before plotting. The Yangtze River and the Yellow River are highlighted in blue curves. Vectors only exceeding the 95% confidence level are shown. White hatchings denote that the anomalies are significant at the 95% confidence level (for observations) or more than 80% of models agree with the sign of the MME (for CMIP models)

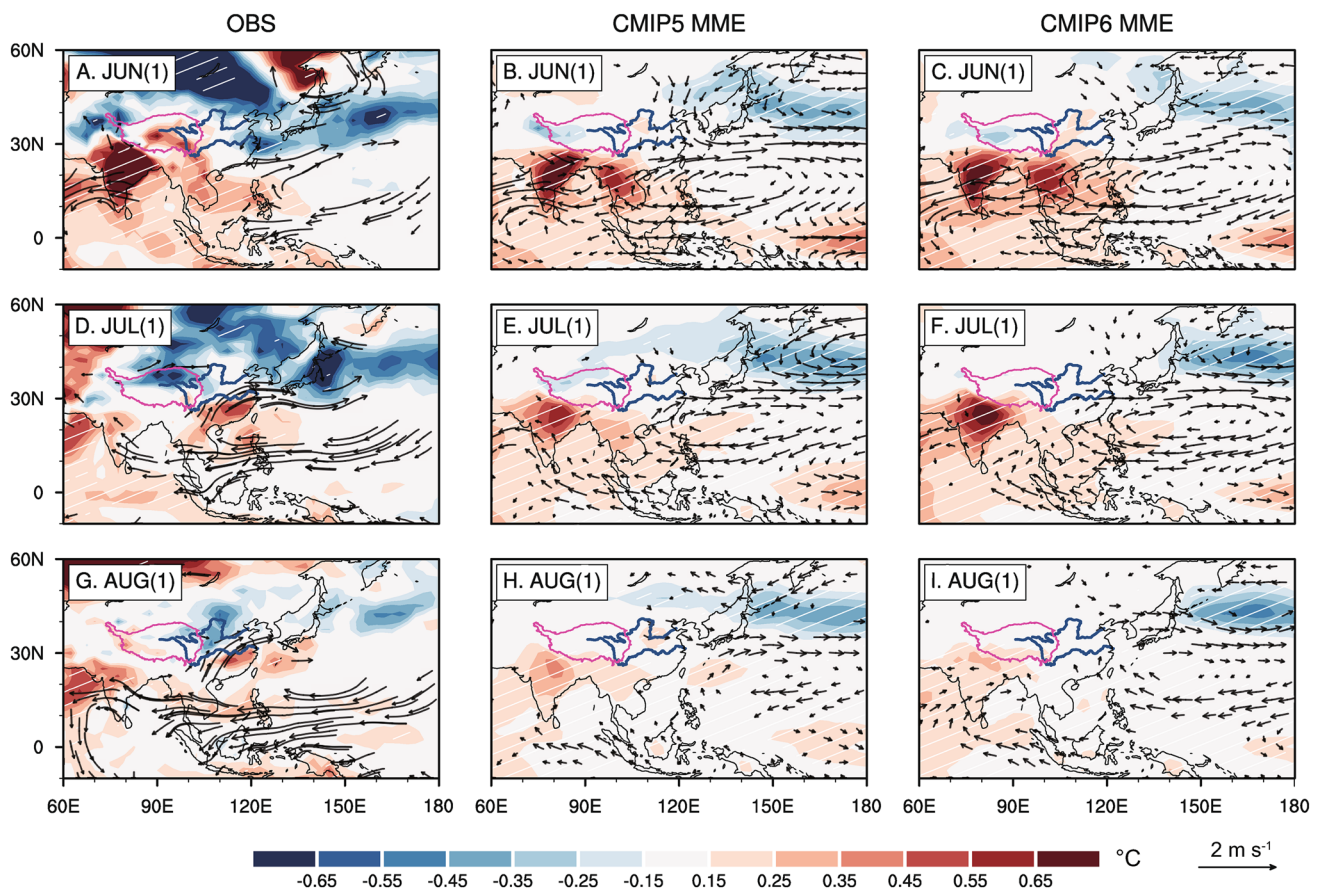


**Fig. 2** Same as Fig. 1, but colors for SAT anomalies (units: °C)

also examine the simulations of AAC persistence during post-EP and post-CP El Niño summers in CMIP models, in an effort to provide insights into the climate impacts induced by ENSO diversity.

The remaining paper is organized as follows. Section 2 describes the data and methods. Section 3 presents a full picture of the biased persistence of summer AAC in CMIP5 and CMIP6 models. A hierarchy of physical mechanisms contributing to the model biases is investigated in Sect. 4. Section 5 provides discussions on the diverse responses of AAC persistence during the post-CP and post-EP El Niño summers in CMIP models. The high-performance CMIP models are also selected in this section, followed by a summary in Sect. 6.

## 2 Data and methods

### 2.1 Data

The observational datasets include the monthly Hadley Centre Sea Ice and SST (HadISST) dataset (Rayner et al. 2003),

Climate Prediction Center Merged Analysis of Precipitation (CMAP) dataset (Xie and Arkin 1997), and the National Centers for Environmental Prediction–National Center for Atmospheric Research (NCEP–NCAR) atmospheric reanalysis (Kalnay et al. 1996) for 1979–2005. We also use the monthly Simple Ocean Data Assimilation ocean/sea ice reanalysis (SODA) ocean state variables, i.e., subsurface potential temperature and ocean current velocity, for the period 1979–2005 (Carton and Giese 2008).

The monthly outputs for 1979–2005 from 36 CMIP5 (Taylor et al. 2012) and 45 CMIP6 (Eyring et al. 2016) models are adopted in the present study (Table 1). Here, we analyze only the first ensemble member (commonly, ‘r1i1p1f1’ for CMIP5 and ‘r1i1p1f1’ for CMIP6) of the historical run of each model. The main conclusions of this study are generally robust against extended study period (i.e., 1979–2014) and varying model numbers. For consistency, all the observations and model simulations are horizontally interpolated onto  $2.5^\circ \times 2.5^\circ$  grids using bilinear interpolation before analysis. In the vertical direction, the observed and simulated oceanic variables are linearly interpolated into the common 82 levels from 10 to 4800 m.

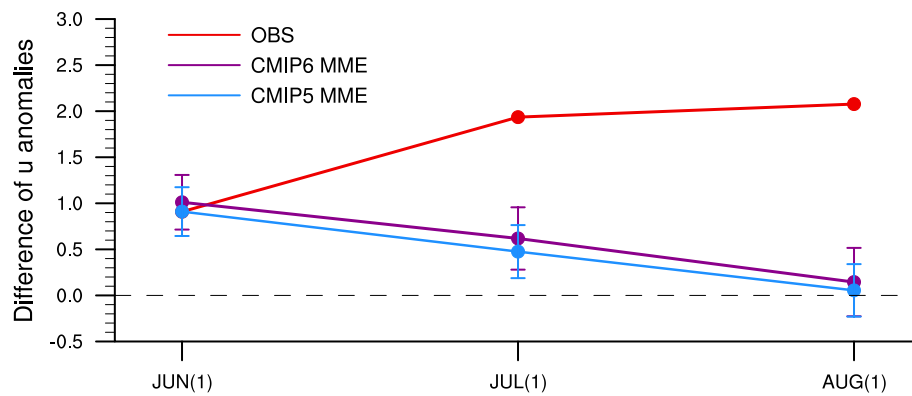


**Fig. 3** Temporal evolutions of the AAC index, i.e., difference of 850-hPa zonal winds between a northern region ( $20^{\circ}$ – $30^{\circ}$ N,  $110^{\circ}$ – $140^{\circ}$ E) and a southern region ( $5^{\circ}$ – $15^{\circ}$ N,  $100^{\circ}$ – $130^{\circ}$ E), for the El Niño composite in observations (red line), CMIP5 MME (light blue line), and

CMIP6 MME (purple line). Error bars for the CMIP5 and CMIP6 MME denote  $\pm$  onefold standard deviation of inter-model variability among 45 CMIP6 and 36 CMIP5 models, respectively

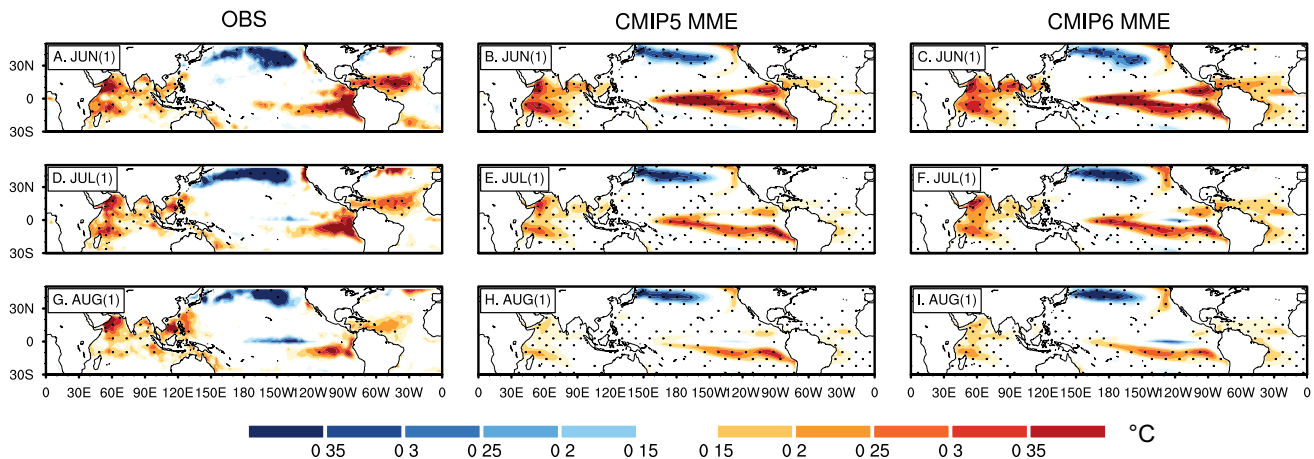


**Fig. 4** SSTA (colors; units:  $^{\circ}$ C) for the El Niño composite in the observations (left panels), CMIP5 MME (middle panels), and CMIP6 MME (right panels) in June(1) (A–C), July(1) (D–F), and August(1) (G–I). Stippling denotes that the anomalies are significant at the 95% confidence level (for observation) or more than 80% of models agree with the sign of the MME (for CMIP models)

## 2.2 Methods

### 2.2.1 Definition of climate indices

We employ D(0)JF(1) Niño-3.4 index to track ENSO variability, which is defined as the SSTA averaged over the central-eastern Pacific ( $5^{\circ}$ S– $5^{\circ}$ N,  $120^{\circ}$ W– $170^{\circ}$ W). Here, suffix 0 and 1 in parentheses refer to ENSO year and its post year, respectively. We define the El Niño years as those when the standardized D(0)JF(1) Niño-3.4 indices are above 0.5. Ten El Niño events (namely 1982/83, 1986/87, 1987/88, 1991/92, 1994/95, 1997/98, 2002/03, 2004/05, 2006/07 and 2009/10) are identified for further study (Supplementary Table S1). Since we concentrate on El Niño-induced inter-annual variability, we subtract the 11-yr running mean from the original datasets before analysis to eliminate decadal

or longer variations. The cold tongue index (CTI), defined as the regional-averaged mean-state SST over the equatorial Pacific cold tongue area ( $3^{\circ}$ S– $3^{\circ}$ N,  $150^{\circ}$ E– $140^{\circ}$ W), is introduced to delineate the equatorial cold tongue bias. The cold tongue is more westward-extended in the model with lower CTI. We use the probability density function (PDF) to depict the likelihood of CTI in CMIP5 and CMIP6 models. Through observing the horizontal shift of PDF, one can judge whether CTI changes significantly under two generations of CMIP models. The kernel density estimation is adopted to fit CTI at monthly scales, which is a non-parametric technique for the PDF estimation of an assigned dataset. The 95% uncertainty ranges (2.5th to 97.5th percentiles) of CTI in CMIP models are estimated via the bootstrapping resampling test (Tang et al. 2022a). Specifically, we compute the 95% uncertainty ranges of CMIP5 and CMIP6 MME by

**Fig. 5** Same as Fig. 3, but for SSTA gradient between NIO and WP (units: °C) from June(1) to August(1)

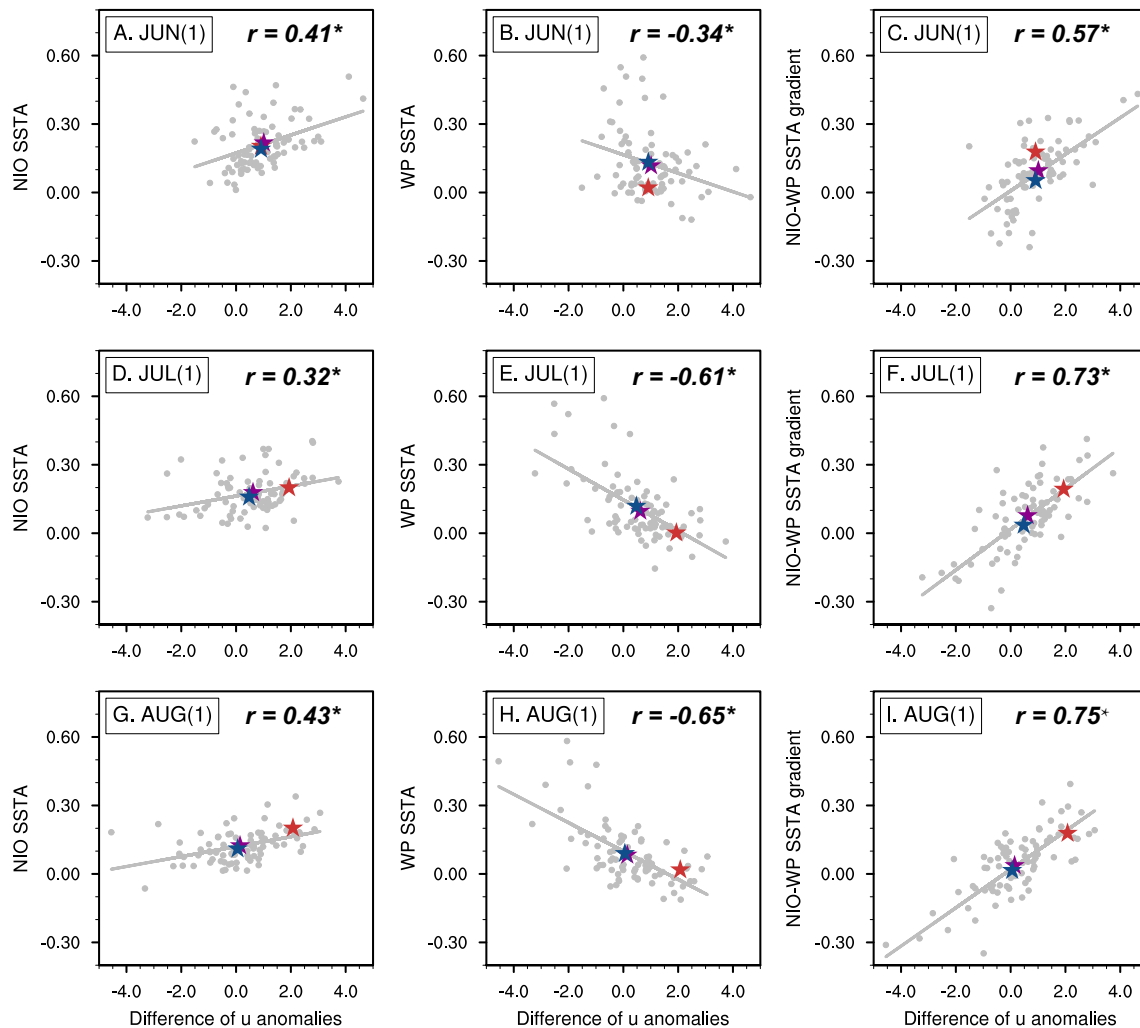
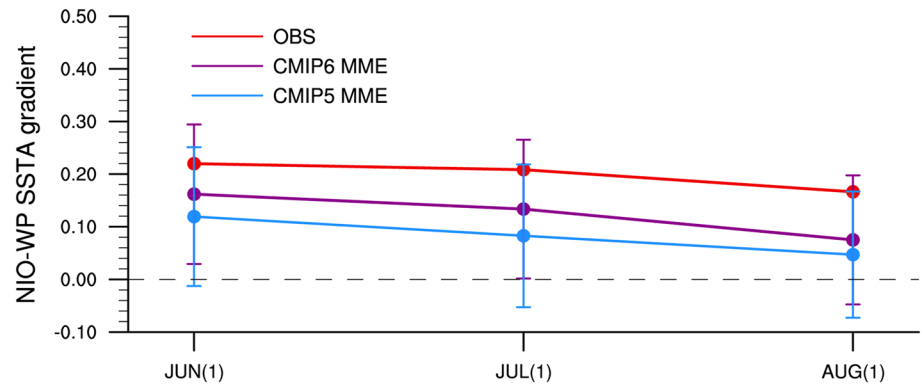


**Fig. 6** Scatterplot between AAC index and SSTA averaged over the NIO ( $0^{\circ}$ – $20^{\circ}$ N,  $50^{\circ}$ – $120^{\circ}$ E; left panels), WP ( $10^{\circ}$ S– $10^{\circ}$ N,  $140^{\circ}$ E– $170^{\circ}$ W; middle panels), and NIO–WP SSTA gradient (right panels) for the El Niño composite in June(1) (A–C), July(1) (D–F), and August(1) (G–I). The grey solid circles denote CMIP mod-

els, while the red, blue and purple stars represent the observations, CMIP5 MME and CMIP6 MME, respectively. The linear regression lines are also shown in each subgraph. The asterisk denotes the regression is statistically significant at  $p < 0.01$  level based on the Student's  $t$ -test

10,000 random samplings (with replacement), respectively. The CMIP6 MME is considered statistically distinct from CMIP5 MME only when CMIP6 MME is not included in the 95% uncertainty ranges of CMIP5 (Planton et al. 2021).

We define the thermocline depth as that of the 20 °C isotherm. The focus of the present study is on post-El Niño summer, i.e., June(1), July(1) and August(1), which is the monsoon season for EA when the IO capacitor comes into effect (Wu et al. 2009; Chen et al. 2016). The composite of SST, precipitation, surface air temperature (SAT), atmospheric and oceanic circulation anomalies during post-El Niño summers are used to represent El Niño-induced variabilities. We also repeat our analyses but regress climate variables against the standardized D(0)JF(1) Niño-3.4 index to examine the results. The multi-model ensemble mean (MME) is calculated as the average of model outputs with equivalent weights, which reflects the overall performance of CMIP models. If more than 80% of models agree with the sign of the MME, we deem it as a statistically significant inter-model agreement. We calculate the statistical significances of composite and regression analyses based on two-sided Student's *t*-test.

### 2.2.2 Three criteria to distinguish EP and CP El Niño events

Considering the robustness of El Niño behaviors may be sensitively affected by the events captured, we adopt three criteria in the present study to distinguish EP and CP El Niño events and compare the composite results. First, we adopt the classification criteria based on D(0)JF(1) Niño-3 (5°S–5°N, 150°W–90°W) and Niño-4 (5°S–5°N, 160°E–150°W) indices to select EP and CP El Niño events (Yeh et al. 2009). An EP (CP) El Niño event is defined when the D(0)JF(1) Niño-3 index is greater (less) than the Niño-4

index. Second, we classify EP and CP El Niño events via the El Niño Modoki index (EMI; Ashok et al. 2007), that is:

$$EMI = [SSTA]_A - 0.5 \times [SSTA]_B - 0.5 \times [SSTA]_C \quad (1)$$

where  $[SSTA]_A$ ,  $[SSTA]_B$ , and  $[SSTA]_C$  indicate regional-mean SSTA over region A (10°S–10°N, 165°E–140°W), region B (15°S–5°N, 110–70°W) and region C (10°S–20°N, 125–145°E), respectively. A CP El Niño event is identified when the EMI is greater than or equal to  $0.8\sigma$  (standard deviation). Third, the cold tongue Niño index (Niño<sub>CT</sub>) and warm pool Niño index (Niño<sub>WP</sub>) are employed to quantify the two types of El Niño quantitatively (Ren and Jin 2011), which are piecewise linear combinations of Niño-3 and Niño-4 indices:

$$\begin{cases} Niño_{CT} = Niño3 - \alpha Niño4 \\ Niño_{WP} = Niño4 - \alpha Niño3 \end{cases}, \quad \alpha = \begin{cases} 0.4, & Niño3 \times Niño4 > 0 \\ 0, & Niño3 \times Niño4 \leq 0 \end{cases} \quad (2)$$

The El Niño events with Niño<sub>WP</sub> greater (less) than Niño<sub>CT</sub> are defined as CP (EP) El Niño events. The selection results in the observation, CMIP5 and CMIP6 models based on three criteria are summarized in the Supplementary Tables S1, S2 and S3.

### 2.2.3 Diagnostic tools

To assess the energy propagation of PJ teleconnection pattern, the horizontal wave-activity fluxes (Takaya and Nakamura 2001) are defined as:

$$W = \frac{1}{2|\bar{V}|} \begin{cases} \bar{U}(\psi'^2_x - \psi'\psi'_{xx}) + \bar{V}(\psi'_x\psi'_y - \psi'\psi'_{xy}) \\ \bar{U}(\psi'_x\psi'_y - \psi'\psi'_{xy}) + \bar{V}(\psi'^2_y - \psi'\psi'_{yy}) \end{cases} \quad (3)$$

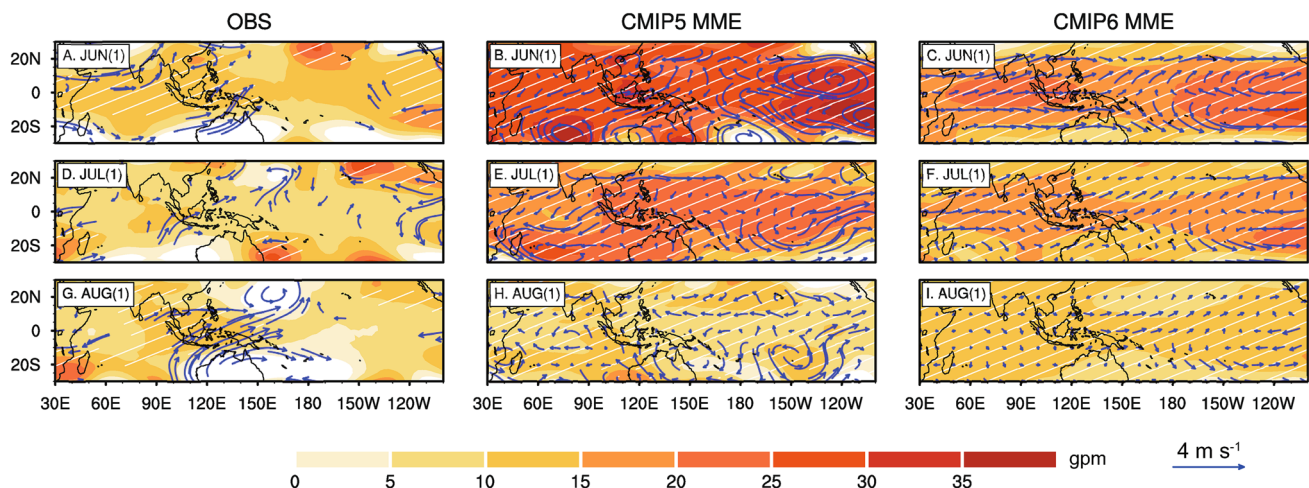


**Fig. 7** Same as Fig. 1, but colors for 200-hPa geopotential height anomalies (units: gpm) and vectors for 200-hPa wind anomalies (units:  $\text{m s}^{-1}$ )

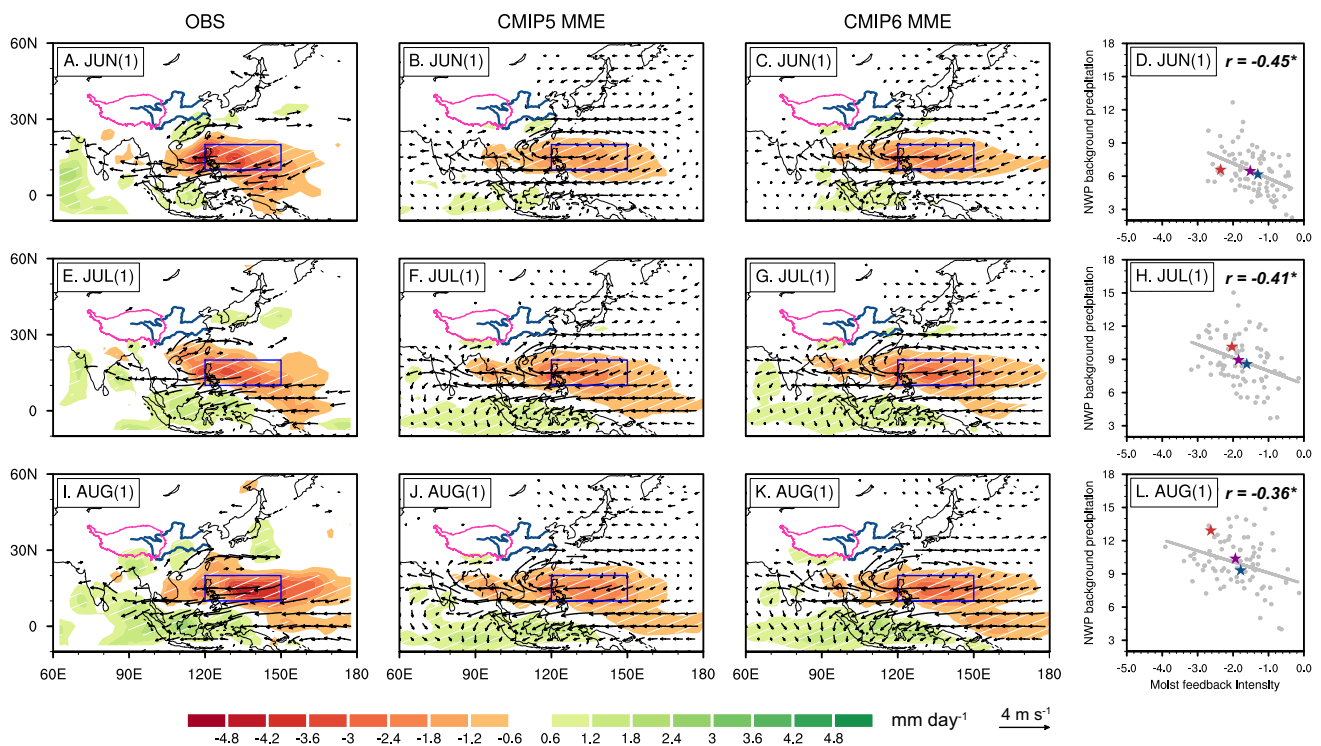


**Fig. 8** 850-hPa wind (vectors; units:  $\text{m s}^{-1}$ ) and precipitation (colors; units:  $\text{mm day}^{-1}$ ) anomalies regressed onto the standardized AAC index in observations (left panels), CMIP5 MME (middle panels), and CMIP6 MME (right panels) in June(1) (A–C), July(1) (E–G), and August(1) (I–K). The Tibetan Plateau is highlighted in pink curve and has been masked out before plotting. The Yangtze River and the Yellow River are highlighted in blue curves, while the key region of moist feedback ( $10^{\circ}$ – $20^{\circ}\text{N}$ ,  $120^{\circ}$ – $150^{\circ}\text{E}$ ) is highlighted in blue box. Vectors only exceeding the 95% confidence level are shown. White hatchings denote that the anomalies are significant

where  $\bar{V}$  is the horizontal wind velocity vector,  $U$  and  $V$  denote the zonal and meridional wind velocity, respectively.  $\psi$  represents the geostrophic stream function. The primes and overbars represent the composite anomalies during post-El Niño summers and background mean-state quantities, respectively.

To illuminate the physical processes underlying SSTA changes, we employ the upper-ocean heat budget (e.g., Xie et al. 2010; Chen et al. 2016) as:

$$\begin{aligned} \partial T' / \partial t = & \frac{Q'}{\rho C_p h} - \bar{u} \frac{\partial T'}{\partial x} - u' \frac{\partial \bar{T}}{\partial x} - \bar{v} \frac{\partial T'}{\partial y} \\ & - v' \frac{\partial \bar{T}}{\partial y} - \bar{w} \frac{\partial T'}{\partial z} - w' \frac{\partial \bar{T}}{\partial z} + D \end{aligned} \quad (4)$$

in which the prime indicates the composite anomaly and the overbar represents the background mean-state quantity.  $T$  and  $\partial T / \partial t$  denote the oceanic potential temperature and its tendency, respectively.  $Q$  represents the net

at the 95% confidence level (for observations) or more than 80% of models agree with the sign of the MME (for CMIP models). Scatterplots between moist feedback intensity (units:  $\text{mm day}^{-1}$ ) and NWP background precipitation (units:  $\text{mm day}^{-1}$ ) in June(1) (D), July(1) (H), and August(1) (L) are shown as well. Larger negative value indicates the stronger moist feedback. The grey solid circles denote CMIP models, while the red, blue and purple stars represent the observations, CMIP5 MME and CMIP6 MME, respectively. The linear regression lines are also shown in each scatterplot. The asterisk denotes the regression is statistically significant at  $p < 0.01$  level based on the Student's  $t$ -test

ocean–atmosphere heat flux including latent heat flux, sensible heat flux, net surface shortwave radiation and net surface longwave radiation (positive value indicates downward surface heat flux, i.e., ocean warming).  $\rho$  ( $= 10^3 \text{ kg m}^{-3}$ ) is the seawater density,  $C_p$  ( $= 4000 \text{ J kg}^{-1} \text{ K}^{-1}$ ) is the ocean specific heat capacity, and  $h$  is the thickness of the ocean mixed layer.  $u$ ,  $v$ , and  $w$  denote ocean current velocity in three dimensions. Since CMIP5 models did not provide  $w$ , we only examine the contributions of  $w$ -related terms in CMIP6 models.  $D$  is the diffusion term. The nonlinear terms are omitted due to trivial influence in this study.

### 3 Weak persistence of AAC and its climate impacts

Figure 1 illustrates the composite monthly 850-hPa wind and precipitation anomalies from June(1) to August(1) in the observations, CMIP5 and CMIP6 MME. The AAC hovering

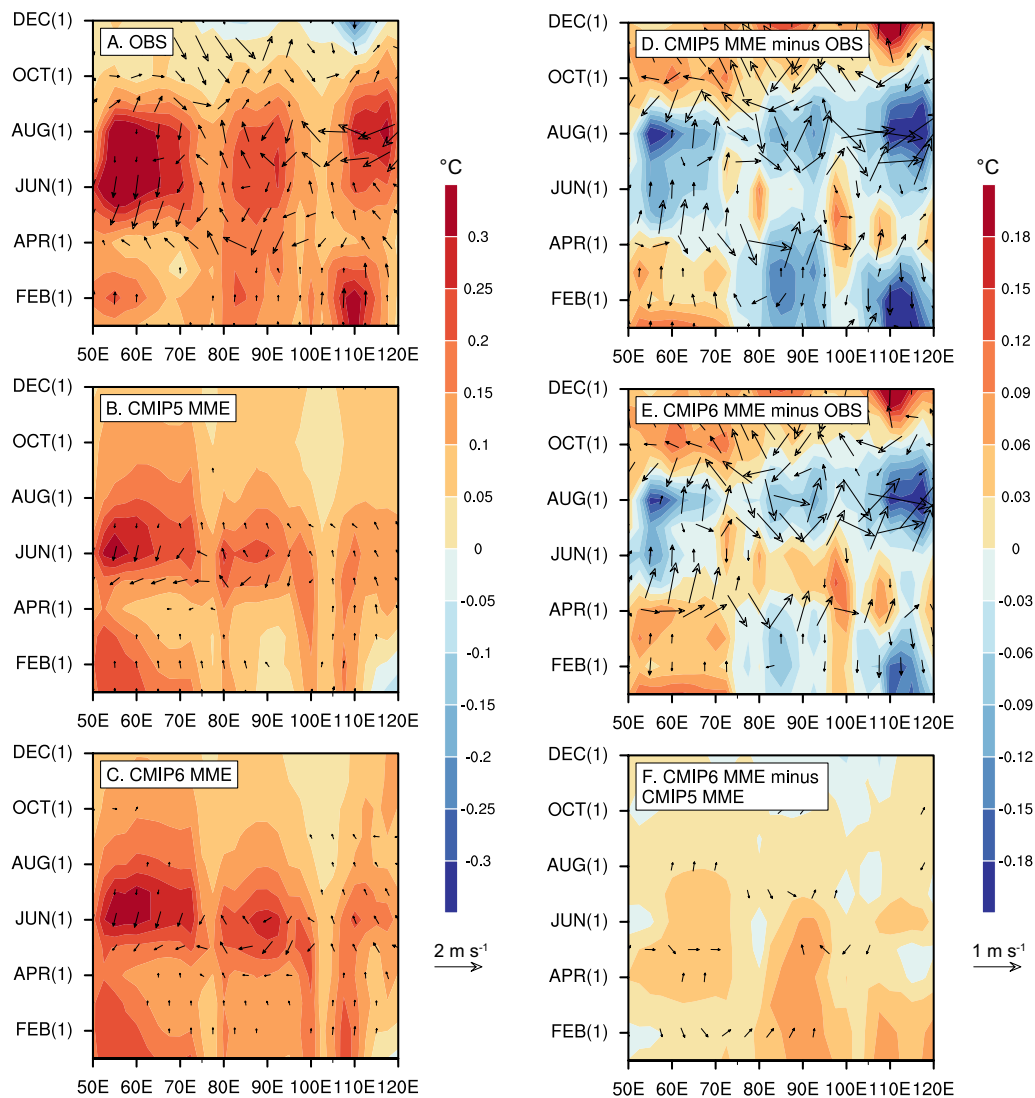


**Fig. 9** Longitude–time section of 0–20°N averaged SSTA (colors; units: °C) and 850-hPa wind anomalies (vectors; units:  $\text{m s}^{-1}$ ) for the El Niño composite in the observation (A), CMIP5 MME (B), CMIP6

MME (C), difference between CMIP5 MME and observation (D), difference between CMIP6 MME and observation (E), and difference between CMIP6 MME and CMIP5 MME (F)

over the Indo–NWP warm pool and its concomitant precipitation response can persist throughout post-El Niño summers in the observations (Fig. 1a, d, g). Both CMIP5 and CMIP6 MME can capture the general characteristics of the AAC pattern in the post-El Niño early summer (Fig. 1b, c, e, f). However, the AAC shifts eastward away from the mainland and fails to maintain over EA in August(1) in CMIP5 and CMIP6 MME (Fig. 1h, i). Similar results can be obtained from the regression analyses (Supplementary Fig. S1G, H, I) and extended time period (Supplementary Fig. S2E, F). We further evaluate each CMIP model individually and find this weak persistence of the simulated summer AAC might be a common model bias (figures not shown).

The observational El Niño-induced precipitation anomalies display a meridional dipole pattern over EA during

post-El Niño summer: rainfall is reduced over the NWP, while enhanced along the Meiyu/Baiu front. Subject to the weak persistence of AAC, the anomalous rain belt extending from the southern part of East China to Korea and South Japan disappears in August(1) in CMIP5 and CMIP6 MME (Fig. 1h, i), exhibiting distinct discrepancies from the observation. Similar results could be obtained from the regression analyses (Supplementary Fig. S1G, H, I). This simulation failure may potentially lead to a limited skill and substantial inter-model uncertainty in the prediction of EA summer monsoon in late summer compared with early summer months. Figure 2 displays the composite monthly 850-hPa wind and SAT anomalies from June(1) to August(1) in the observations, CMIP5 and CMIP6 MME. We observe the above-normal SAT anomalies in South China and

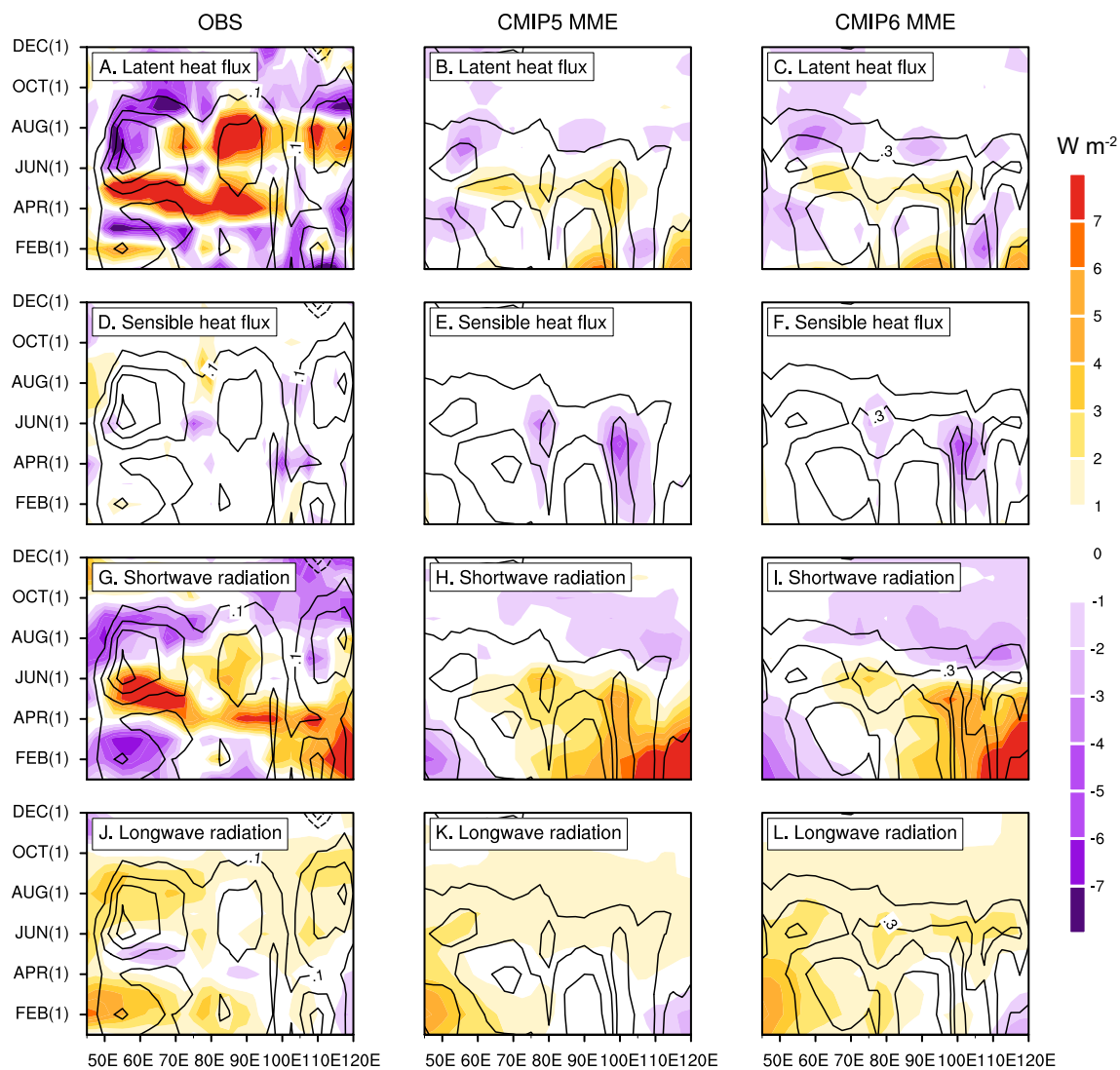


**Fig. 10** Longitude–time section of 0–20°N averaged SSTA (contours; units: °C), latent heat flux (shading; units:  $\text{W m}^{-2}$ ), sensible heat flux (shading; units:  $\text{W m}^{-2}$ ), shortwave radiation (shading; units:  $\text{W m}^{-2}$ ), and longwave radiation (shading; units:  $\text{W m}^{-2}$ ) anomalies for the El

Niño composite in the observations (left panels), CMIP5 MME (middle panels), and CMIP6 MME (right panels). Solid and dashed contours are at interval of 0.1 ( $\pm 0.1, \pm 0.2, \pm 0.3, \dots$ )

Indo–China peninsula accompanied by AAC in August(1) in the observations (Fig. 2g). However, the anomalous SAT patterns are vastly diminished in August(1) in CMIP5 and CMIP6 MME (Fig. 2h, i). Similar phenomenon can be observed from the regression analyses (Supplementary Fig. S3G, H, I).

We further diagnose the energy propagation of PJ pattern from June(1) to August(1) in the observations, CMIP5 and CMIP6 MME. The low-level poleward energy propagations over tropical NWP are relatively weaker in CMIP models in August(1) compared with their observational counterpart (Supplementary Fig. S4G, H, I). To quantitatively depict the monthly evolutions of summer AAC, we define the AAC index as the difference of 850-hPa zonal winds between a

northern region ( $20^{\circ}$ – $30^{\circ}\text{N}$ ,  $110^{\circ}$ – $140^{\circ}\text{E}$ ) and a southern region ( $5^{\circ}$ – $15^{\circ}\text{N}$ ,  $100^{\circ}$ – $130^{\circ}\text{E}$ ) (Wang and Fan 1999; Jiang et al. 2017). In the observations, the AAC intensity is stronger in July(1) and August(1) than in June(1) (Tang et al. 2021). Nevertheless, the AAC persists weakly in CMIP5 and CMIP6 MME, indicating that CMIP models fail to reproduce the evolution of summertime AAC (Fig. 3). This weak persistence bias will further lead to the weak magnitude bias of summer mean AAC. CMIP6 MME simulates a more realistic AAC evolution than its CMIP5 counterpart during post-El Niño summer, albeit still at relatively low level. We also use another AAC index, i.e., regional-averaged 850-hPa relative vorticity anomalies over the tropical NWP ( $10^{\circ}$ – $35^{\circ}\text{N}$ ,  $120^{\circ}$ – $160^{\circ}\text{E}$ ; Wu et al. 2010). The conclusion remains robust

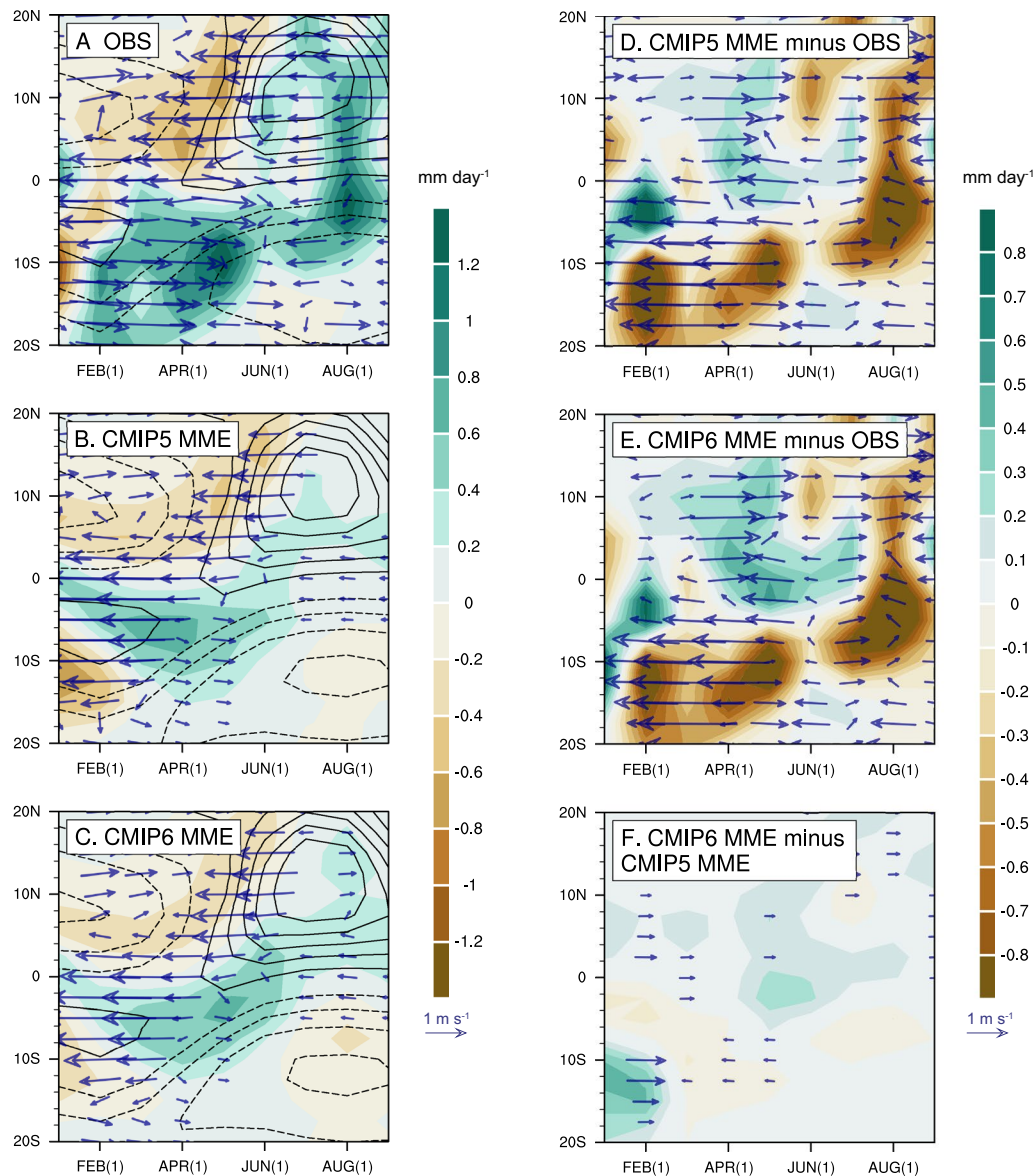


**Fig. 11** Time–latitude section of  $40^{\circ}$ – $100^{\circ}$ E averaged precipitation anomalies (colors; units:  $\text{mm day}^{-1}$ ) and 850-hPa wind anomalies (vectors; units:  $\text{m s}^{-1}$ ) for the El Niño composite in the observation (A), CMIP5 MME (B), CMIP6 MME (C), difference between CMIP5 MME and observation (D), difference between CMIP6 MME

and observation (E), and difference between CMIP6 MME and CMIP5 MME (F). The black contours in A–C denote 850-hPa background zonal wind climatology (interval at  $2 \text{ m s}^{-1}$  with westerly wind by solid contours, easterly wind by dashed contours, and zero omitted)

against different AAC index definitions (Supplementary Fig. S5). In the next section, we will investigate the role of SSTA in each ocean basin to comprehend the physical origins of the biased persistence of AAC in more detail.

## 4 Physical mechanisms

### 4.1 Weak persistence of NIO–WP SSTA gradient

Figure 4 demonstrates the composite monthly SSTA from June(1) to August(1) in the observations, CMIP5 and CMIP6 MME. The SSTA in the IO feature IOB warming throughout post-El Niño summer in the observations (Fig. 4a, d, g). The IOB warming patterns in CMIP5 and CMIP6 MME are comparable to the observations in the post-El Niño early summer (Fig. 4b, c, e, f). However, they are significantly weaker

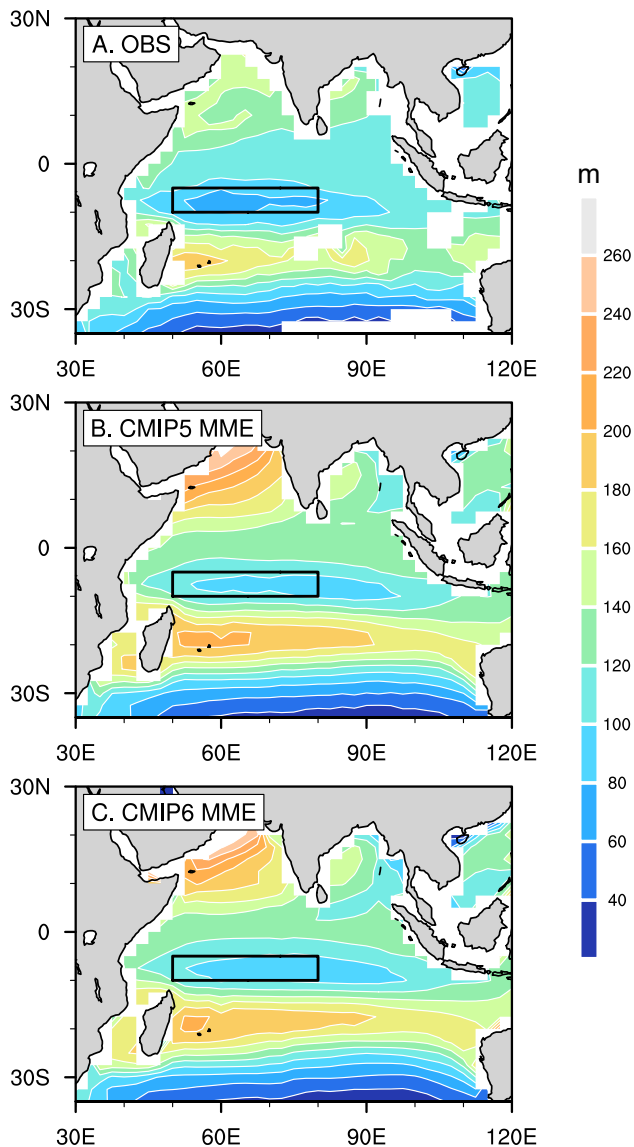


**Fig. 12** Climatological mean thermocline depth (colors; units: m) in the IO from March to May in the observation (A), CMIP5 MME (B), and CMIP6 MME (C). The SWIO thermocline dome region (10°S–5°S, 50°E–80°E) is highlighted in black box

than those in the observational August(1), indicating a weak persistence of IOB warming (Fig. 4h, i). In addition, the equatorial Pacific decaying El Niño-related SSTA penetrate too far westward in CMIP5 and CMIP6 MME than their observational counterpart, and could persist over the tropical west Pacific (WP) during the entire post-El Niño summer. The above two SSTA biases can be observed from the regression analyses (Supplementary Fig. S6) and extended time period (Supplementary Fig. S7) as well.

Following previous studies (Ohba and Ueda 2006; He and Zhou 2015; Jiang et al. 2017, 2019), we construct the inter-basin SSTA gradient index as SSTA differences between

North IO (NIO; 0°–20°N, 50°–120°E) and WP (10°S–10°N, 140°E–170°W). Figure 5 shows the monthly evolutions of NIO–WP SSTA gradient in the observations, CMIP5 and CMIP6 models. Due to the rapidly decaying IOB warming and long-lasting WP warming bias during post-El Niño summers, the NIO–WP SSTA gradients persist weakly in CMIP5 and CMIP6 MME compared with their observational counterpart. The SSTA gradient is relatively better simulated in CMIP6 MME than in CMIP5 MME, corresponding to the performance improvement of summer AAC. To confirm the relationship between AAC index and NIO–WP SSTA gradient, the corresponding scatterplots from June(1) to August(1) are displayed in Fig. 6. The AAC magnitudes are correlated with NIO warming throughout post-El Niño summers, with relatively high inter-model correlations of 0.41, 0.32 and 0.43 in June(1), July(1) and August(1), respectively ( $n = 83, p < 0.01$ ). In addition, the AAC magnitudes are negatively associated with the unrealistic WP warming from June(1) to August(1), indicating that the model with stronger WP warming bias tend to reproduce weaker AAC during post-El Niño summers. Their inter-model correlations are  $-0.34$ ,  $-0.61$  and  $-0.65$  in June(1), July(1) and August(1), respectively ( $n = 83, p < 0.01$ ). The stronger correlations indicate that the long-lasting WP warming bias may play a more important role than the weakly persistent NIO warming in discontinuing the AAC persistence in post-El Niño late summers. The inter-model correlation coefficients between AAC index and NIO–WP SSTA gradient further improve, reaching 0.57, 0.73 and 0.75 in June(1), July(1) and August(1), respectively ( $n = 83, p < 0.01$ ). It connotes that the simulated NIO–WP SSTA gradient may be the key factor of the inter-model spread of AAC magnitude during post-El Niño summer months.

How does the NIO–WP SSTA gradient affect the lower-level AAC during post-El Niño summers? Fig. 7 presents the composite monthly 200-hPa wind and geopotential height anomalies from June(1) to August(1) in the observations, CMIP5 and CMIP6 MME. In the observations, the 200-hPa geopotential height anomalies, as the proxy of tropospheric temperature anomalies, display a Matsuno–Gill (Matsuno 1966; Gill 1980) pattern over the tropical IO throughout post-El Niño summer. The atmospheric warm Kelvin waves along the equator penetrate into WP, with upper-level westerly anomalies dominating over the Maritime Continent (Fig. 7a, d, g). Nevertheless, the unrealistic warm SSTA in WP in CMIP models can strengthen the local convection/rainfall activities and induce upper-level easterly anomalies on the western side, resulting in weak upper-level wind responses over the Maritime Continent (Fig. 7h, i). This phenomenon can also be observed from the regression analyses (Supplementary Fig. S8H, I). In the lower troposphere, an anomalous cyclonic circulation emerges over the tropical NWP as the Rossby wave response to unrealistic

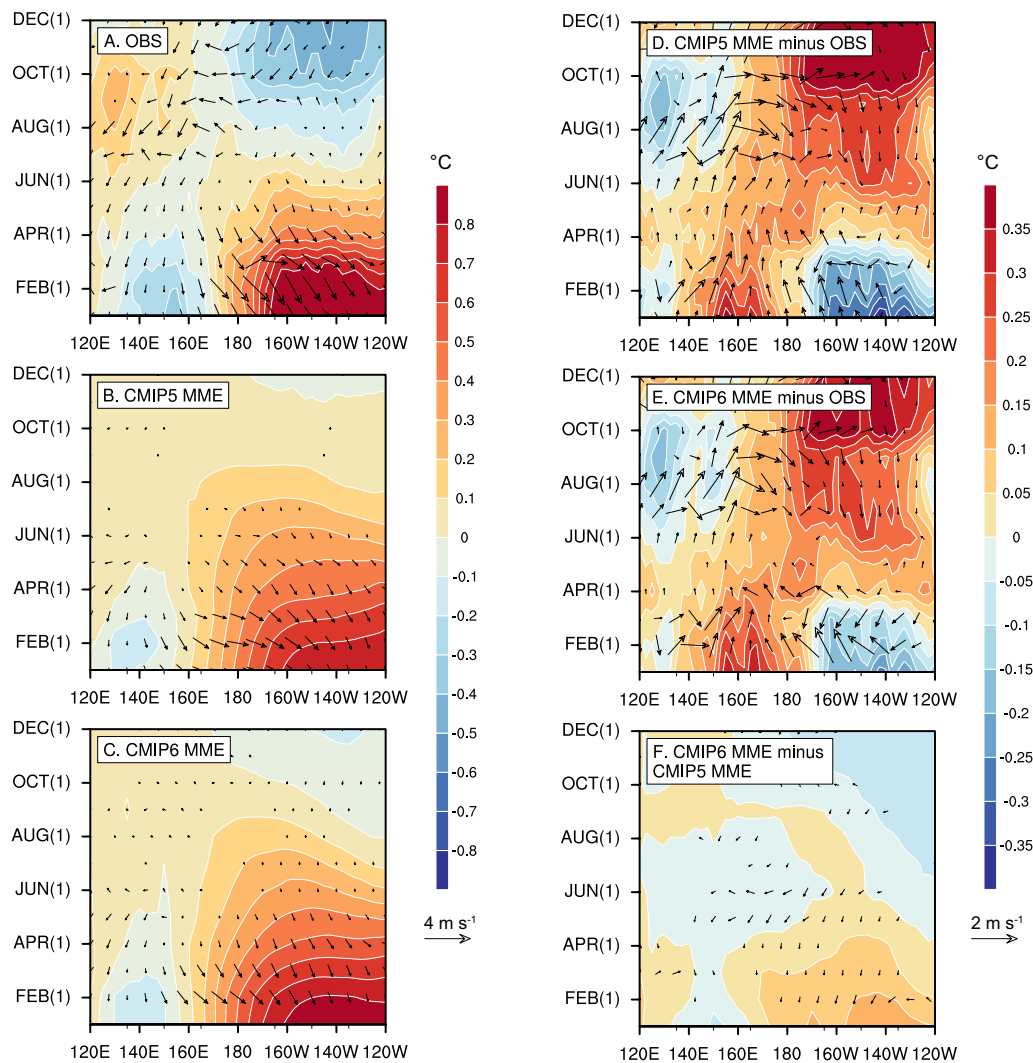


**Fig. 13** Same as Fig. 9, but for 10°S–10°N averaged anomalies in the Pacific

WP warming bias (Fig. 1h, i). The WP warming-induced westward spreading atmospheric Rossby wave will attenuate the NIO warming-induced eastward propagating equatorial Kelvin wave. The weakening extent is possibly determined by the NIO–WP SSTA gradient. Therefore, the weakly persistent NIO–WP SSTA gradient may finally result in the weak persistence of AAC during post-El Niño summers in CMIP5 and CMIP6 models.

Apart from the influence of SSTA gradient, the NWP mean-state changes also play a critical role in the sub-seasonal evolution of summer AAC (Xiang et al. 2013; Hu et al. 2019). Supplementary Fig. S9 shows the mean-state precipitation over EA–NWP from June to August in the observations, CMIP5 and CMIP6 MME. In general, the CMIP models could reasonably reproduce the onset and eastward advance of mean-state NWP summer monsoon, albeit with relatively weak magnitudes. As indicated by Xie et al. (2009), the extent to which the SSTA can influence NWP

circulation anomalies depends on the NWP background mean-state precipitation. The models with stronger mean-state NWP precipitation tend to reproduce intensified moist feedback between local convection and circulation anomalies, thereby enhancing AAC patterns. Hence, even though the SSTA weakens slightly from post-El Niño early to late summer, AAC can still intensify in the observation (Fig. 3). This intensification can be partly attributed to the onset of background NWP summer monsoon in the late summer, which results in enhanced condensational heating anomalies (Wu et al. 2010; Tang et al. 2021). Here, we regress the 850-hPa wind and precipitation onto the standardized AAC index in each grid point to quantify the local moist/convection–circulation feedback (Fig. 8). We define the moist feedback intensity as the regional-mean regressed precipitation anomalies over the key region of moist feedback (10°–20°N, 120°–150°E). The moist feedback intensity shows a generally good relationship with NWP background mean-state

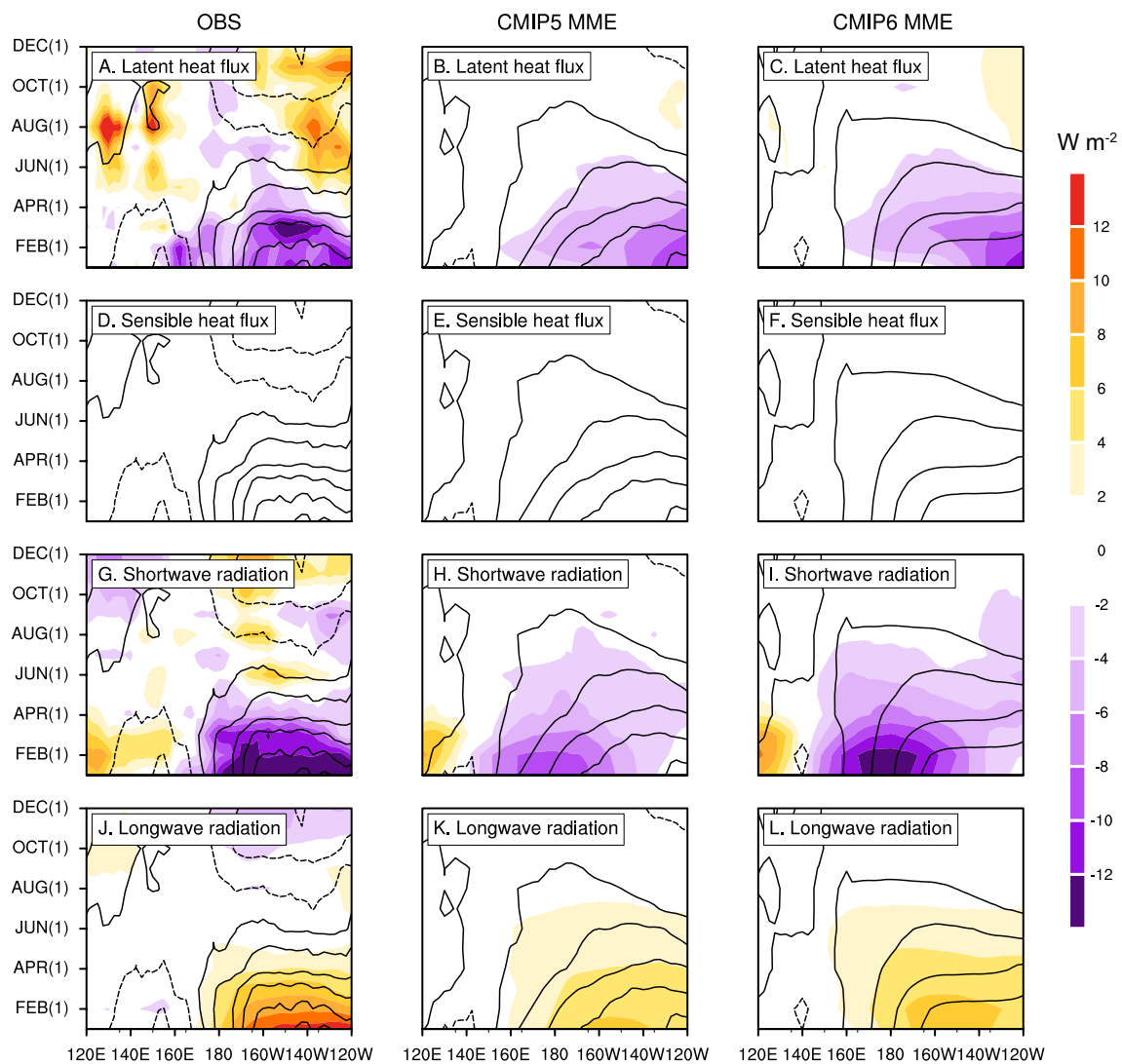


**Fig. 14** Same as Fig. 10, but for 10°S–10°N averaged anomalies in the Pacific. Solid and dashed contours are at interval of 0.2 ( $\pm 0.1, \pm 0.3, \pm 0.5, \dots$ )

precipitation, consistent with previous studies (Wang et al. 2021). However, we also note that the increase of moist feedback intensity from early to late summer is weaker in CMIP5 and CMIP6 MME compared with the observation (Fig. 8d, h, l), which can be attributed to the weaker onset the simulated NWP summer monsoon (Supplementary Fig. S9). The result still holds when we slightly enlarge or shrink the chosen region. Therefore, the weakened increase of moist/convection–circulation feedback intensity may not be able to provide enough support for the intensification of AAC in August(1) in CMIP models as that in the observation. To further probe the relative contributions of SSTA gradient and local mean-state changes, the scatter diagram between AAC index and moist feedback intensity is given (Supplementary Fig. S10). The poorly simulated relationship in the post-El Niño late summer implies a much more important

contribution of the decaying NIO–WP SSTA gradient than that of the weakened increase of moist feedback to the biased persistence of summer AAC in CMIP models.

#### 4.2 Weak persistence of IOB warming

Figure 9 presents the longitude–time section of 0–20°N averaged El Niño-related SSTA and 850-hPa wind anomalies in the IO in the observations, CMIP5 MME, CMIP6 MME, as well as their corresponding differences. The IOB warming is generally less persistent during post-El Niño summers in CMIP5 and CMIP6 MME compared with the observation (Fig. 9d, e). We also observe an overall improvement in IOB warming simulation in CMIP6 MME relative to the CMIP5 MME (Fig. 9f). Why does the IOB warming in CMIP5 and CMIP6 MME could not persist into post-El Niño late

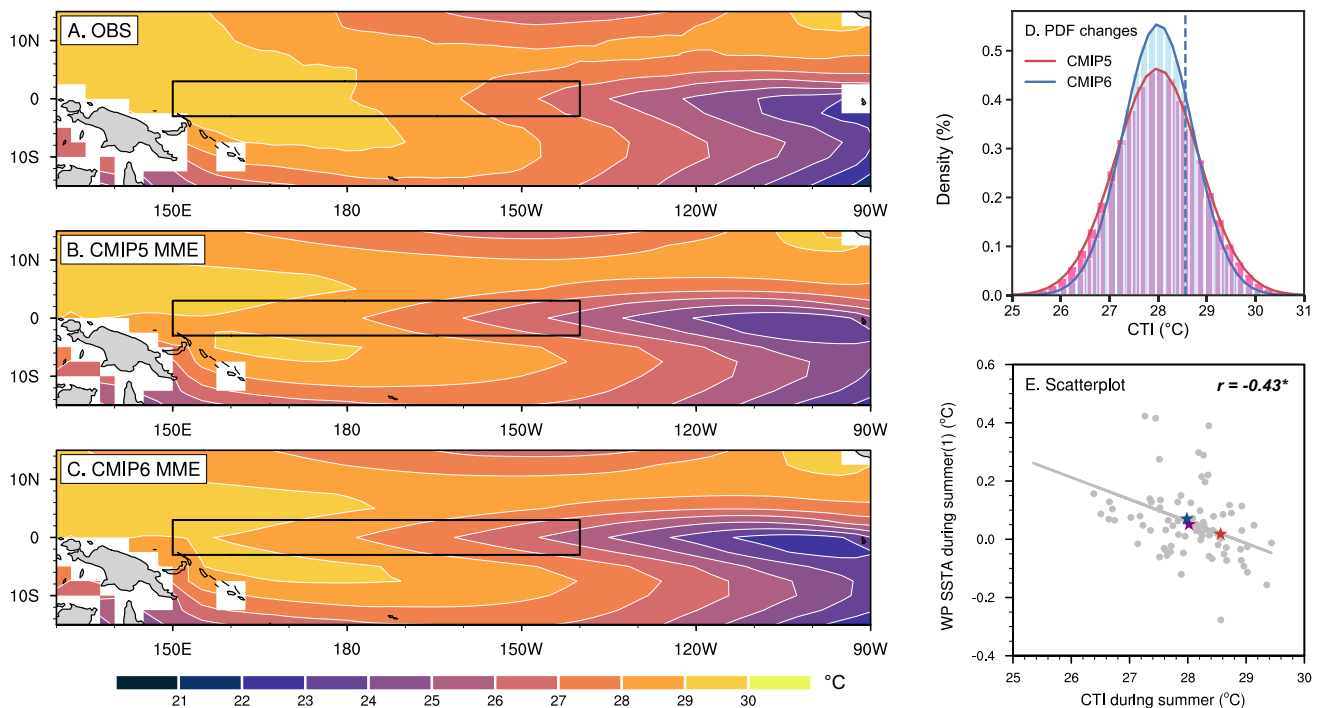


**Fig. 15** Climatological mean SST (colors; units: °C) in the tropical Pacific averaged from June to August in the observations (A), CMIP5 MME (B), and CMIP6 MME (C). The cold tongue region (3°S–3°N, 150°E–140°W) is highlighted in black box. The PDFs of CTI (D) for CMIP5 models (red) and CMIP6 models (blue). The dotted blue line denotes the observation. Scatterplot (E) between the climatological mean SST over the equatorial Pacific cold tongue averaged from

June to August and El Niño-induced SSTA over WP (10°S–10°N, 140°E–170°W) averaged from June(1) to August(1). The grey solid circles denote CMIP models, while the red, blue and purple stars represent the observations, CMIP5 MME and CMIP6 MME, respectively. The linear regression line and correlation coefficient are shown as well

summer? Fig. 10 exhibits the contributions of latent heat flux, sensible heat flux, shortwave radiation, and longwave radiation anomalies to NIO warming. In the observation, the anomalous latent heat flux and shortwave radiation play the more important roles than the other two terms in NIO warming during post-El Niño spring and summer (Fig. 10a, d, g, j), consistent with previous studies (Tao et al. 2016). However, the simulated positive latent heat flux and shortwave radiation anomalies could not persist into post-El Niño late summer (Fig. 10b, c, h, i), resulting in the less persistent IOB warming. The contributions of the oceanic dynamic terms (four oceanic horizontal advection terms) to NIO warming are relatively small (Supplementary Fig. S11).

To further probe the cause of less persistent positive latent heat flux anomalies in CMIP models, the time–latitude section of 40°–100°E averaged El Niño-related precipitation and wind anomalies in the observations, CMIP5 and CMIP6 MME are shown in Fig. 11. The observational precipitation anomalies exhibit wet (dry) center south (north) of the equator during post-El Niño spring, accompanied by the cross-equatorial C-shaped wind anomalies (Fig. 11a). The northern branch of the C-shaped wind anomalies over NIO could persist into subsequent summer seasons, which

plays a key role in the persistence of positive latent heat flux anomalies (Wu et al. 2008; Du et al. 2009). However, the cross-equatorial antisymmetric spring wind patterns are poorly captured in the CMIP5 and CMIP6 MME (Fig. 11d, e). How do the cross-equatorial antisymmetric wind patterns form and why are they weakly simulated in CMIP models? In the observation, the El Niño-induced anomalous anticyclonic circulations in the southeast IO trigger downwelling oceanic Rossby waves propagating westward in D(0)JF(1). The Rossby waves reach the tropical Southwest IO (SWIO; 10°S–5°S, 50°E–80°E) after one season where the shallow background thermocline dome locates. As a result, the local thermocline is deepened, further leading to the SWIO warming during post-El Niño spring (Xie et al. 2002). The SWIO positive SSTA-induced rainfall anomalies excite the cross-equatorial antisymmetric wind pattern during post-El Niño spring, the northern branch of which (i.e., anomalous northeasterly) favors NIO warming after the background mean-state southwesterly monsoon onset in May through the WES feedback (Du et al. 2009). Finally, the observational IOB warming can persist through the entire post-El Niño summer (Fig. 4g).

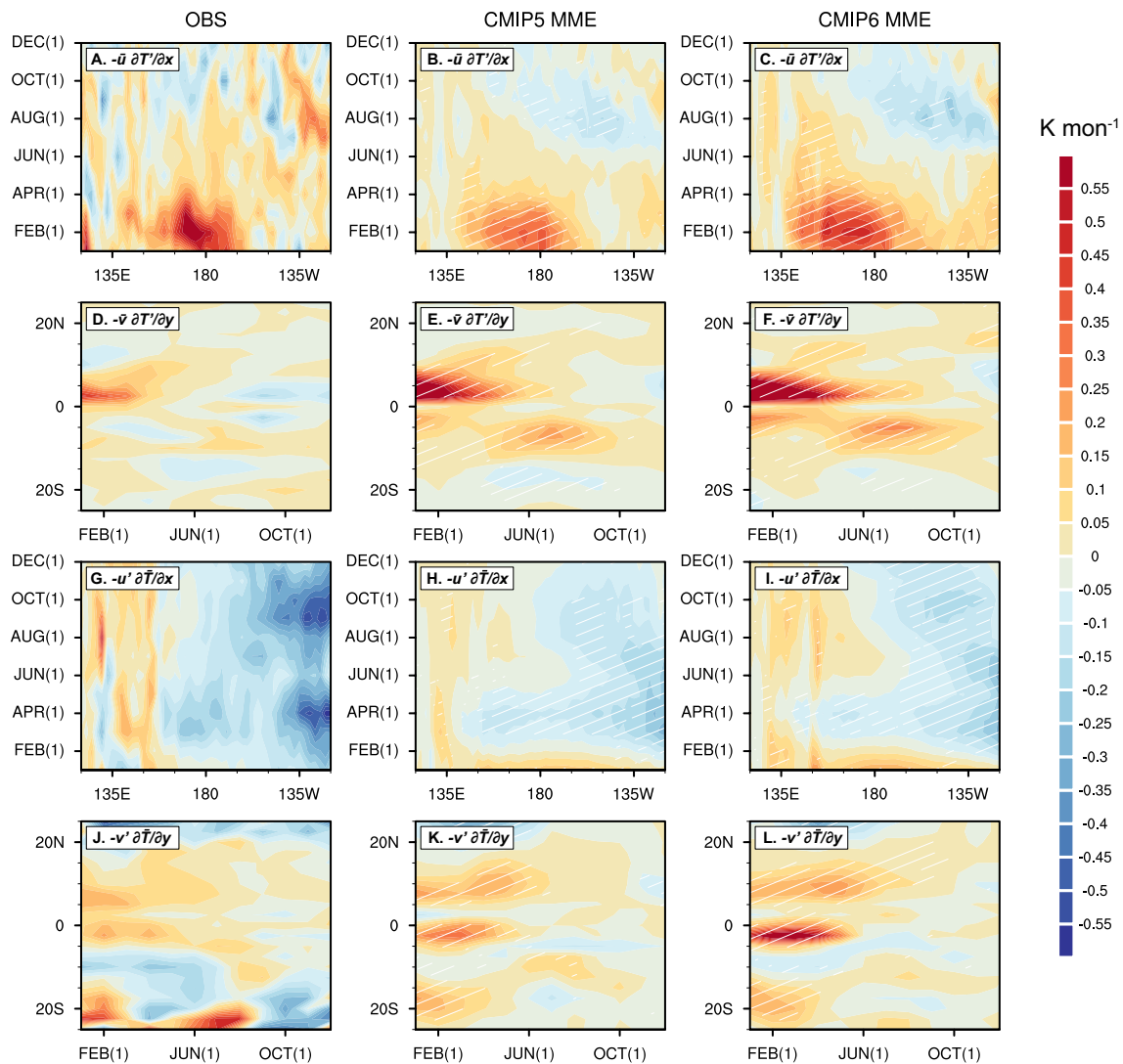


**Fig. 16** Longitude–time section of 10°S–10°N averaged vertical integrations of mean zonal advection of anomalous potential temperature gradient ( $-\bar{u}\partial T'/\partial x$ ; A–C; units:  $\text{K mon}^{-1}$ ), time–latitude section of 140°–180°E averaged mean meridional advection of anomalous potential temperature gradient ( $-\bar{v}\partial T'/\partial y$ ; D–F; units:  $\text{K mon}^{-1}$ ), longitude–time section of 10°S–10°N averaged anomalous zonal advection of mean potential temperature gradient ( $-\bar{u}'\partial \bar{T}/\partial x$ ; G–I; units:

$\text{K mon}^{-1}$ ), and time–latitude section of 140°–180°E averaged anomalous meridional advection of mean potential temperature gradient ( $-\bar{v}'\partial \bar{T}/\partial y$ ; J–L; units:  $\text{K mon}^{-1}$ ) in the ocean mixed layer for the El Niño composite in the observation (left panels), CMIP5 MME (middle panels), and CMIP6 MME (right panels). White hatchings denote that more than 80% of models agree with the sign of the MME (for CMIP models)

Nevertheless, CMIP models suffer from the deeper background mean-state SWIO thermocline depths. Specifically, the regional-mean SWIO thermocline depth during spring (March–May) is only 83.25 m in the observations, whereas it reaches 101.63 m in CMIP5 MME and 98.41 m in CMIP6 MME (Fig. 12). Previous studies indicated that the oceanic Rossby wave-induced thermocline disturbance could hardly affect the SSTa when the background mean-state thermocline is deep (Li et al. 2015; Zheng et al. 2016). In that case, the deepened thermocline-induced SWIO rainfall anomalies in CMIP models will become weak. Thus, the deep thermocline bias in CMIP

models may finally result in drying (wetting) bias with weaker northwesterly (northeasterly) wind anomalies in the southern (northern) equatorial IO (Fig. 11b, c). The dampened wind anomalies, especially the northeasterly wind anomalies north of the equator, further lead to the weak persistence of positive latent heat flux anomalies via the weakened WES feedback (Fig. 10b, c).

Where does the deep thermocline bias in CMIP models originate from? Previous studies have indicated that the CGCMs normally suffer from the so-called IO Dipole-like biases, which feature annual mean easterly wind biases on the equator (Lee et al. 2013; Li et al. 2015; Zheng et al.

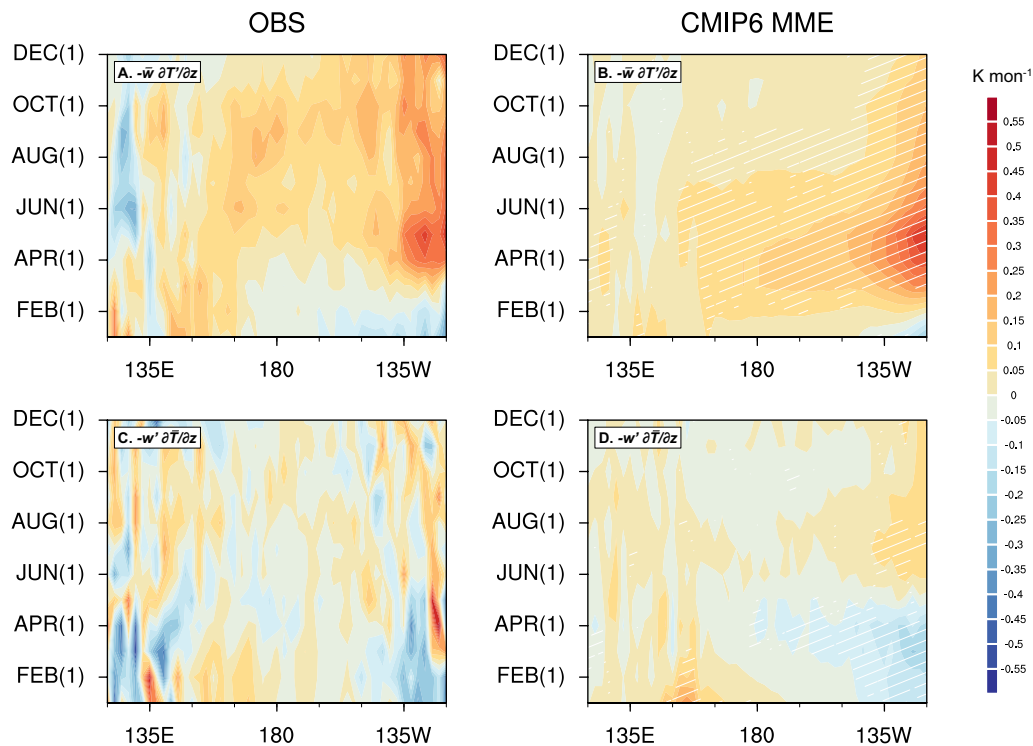


**Fig. 17** Longitude–time section of 10°S–10°N averaged vertical integrations of thermocline feedback ( $-\overline{w'\partial T'/\partial z}$ ; A–B; units: K mon<sup>-1</sup>) and upwelling feedback ( $-\overline{\omega'\partial T/\partial z}$ ; C–D; units: K mon<sup>-1</sup>) in the ocean mixed layer for the El Niño composite in the observation (left

panels) and CMIP6 MME (right panels). White hatchings denote that more than 80% of models agree with the sign of the MME (for CMIP6 models)

2016). The mean-state surface winds in the equatorial IO play an important role in the establishment of the thermocline dome in the SWIO. The model with stronger (weaker) background westerly wind along the equator tends to reproduce strengthened (weakened) surface cyclonic wind curls and upwelling Ekman pumping, thereby a shoaling (deepening) SWIO thermocline dome. Therefore, the mean-state equatorial easterly wind biases result in the deep thermocline biases in the SWIO, finally leading to a less persistent IOB warming.

In addition to the cross-equatorial C-shaped wind-anchored IOB warming, the inter-basin positive feedback between IOB warming and AAC pattern is also crucial to the maintenance of IOB warming (Kosaka et al. 2013; Xie et al. 2016). In the observations, the easterly anomalies on the southern periphery of AAC extend westward to NIO in August(1). They will relax the mean-state southwesterly monsoon and suppress surface evaporation, which is instrumental in surface warming over NIO and south China sea (Fig. 10a). Moreover, the AAC can reduce cloud amount and enhance insolation over Bay of Bengal and the northern south China sea, contributing to the local warming (Fig. 10g). The enhanced IOB warming can in turn strengthen the AAC via the IO capacitor effect, forming the positive feedback. Nevertheless, the simulated AAC

spanning the Indo–NWP warm pool decouples with IOB warming in August(1) in CMIP models. This decoupling finally results in the vanishment of additional NIO warming (Fig. 10b, c, h, i).

### 4.3 Long-lasting WP warming bias

Figure 13 shows the longitude–time section of 10°S–10°N averaged El Niño-related SSTa and wind anomalies over the Pacific in the observations, CMIP5 MME, CMIP6 MME, and their corresponding differences. The differences between CMIP5/6 MME and observations exhibit a long-lasting positive warming center over equatorial WP, known as the excessively westward-extended El Niño-related warming bias (Fig. 13d, e). We also note a reduced excessive westward extension of WP warming bias in CMIP6 MME compared with their CMIP5 counterparts during post-El Niño summer (Fig. 13f). To further illustrate the origins of the long-lasting WP warming bias, we first conduct a diagnostic analysis on sea surface heat flux (Fig. 14). We find that the El Niño warming-induced negative latent heat flux and shortwave radiation anomalies are detrimental to the maintenance of positive SSTa, whereas positive longwave radiation anomalies may not be able to hold the balance. We also note that the simulated shortwave radiation anomalies are

more westward-extended compared with their observational counterpart, possibly because that the mean-state SST in the warm pool region is higher and easier to trigger convection anomalies. To sum up, thermodynamic processes (i.e., sea surface heat flux anomalies) alone could not explain this long-lasting WP warming bias throughout post-El Niño summers. The oceanic dynamical processes may be vitally important for the artificial equatorial WP warming during post-El Niño summers in CMIP models (Tao et al. 2018; Jiang et al. 2021).

Figure 15 presents the background mean-state SST averaged from June to August in the observations, CMIP5 and CMIP6 MME in the tropical Pacific. In the observations, the tropical equatorial Pacific features a zonally asymmetric pattern with a cold tongue (warm pool) in the east (west) (Fig. 15a). However, the simulated equatorial cold tongue is too cold and too far westward-extended, known as the equatorial Pacific zonal SST bias (hereafter cold tongue bias) in CMIP models (Fig. 15b, c). The strong persistence of cold tongue bias may be traced back to the misrepresentation of tropical ocean–atmosphere interaction in the Pacific Ocean (Li and Xie 2014). The regional-mean CTI during summer is 28.56 °C in the observations, whereas it drops to 27.98 and 28.02 °C in CMIP5 and CMIP6 MME, respectively. Relative to CMIP5 models, we observe a slight warming shift and less diversity of CTI PDF in CMIP6 models (Fig. 15d). This indicates a general reduction of the cold tongue bias over WP in CMIP6 models than in CMIP5 models (Grose et al. 2020; Jiang et al. 2021). Nevertheless, this improvement cannot pass the bootstrap resampling test since the 95% uncertainty ranges of CMIP5 encompass CMIP6 MME. Therefore, we infer that the summer cold tongue bias improvement may not be statistically significant from CMIP5 to CMIP6, consistent with Planton et al. (2021).

Previous studies suggested that models with stronger cold tongue bias tend to displace westward the simulated El Niño-related warming pattern along the equatorial Pacific (Jiang et al. 2021). The scatter diagram of summer CTI versus JJA(1) WP warming bias among CMIP models also indicates a generally good relationship between them (Fig. 15e). To shed light on the physical linkages between equatorial Pacific mean-state cold tongue bias and strong persistence of spurious WP SSTA, the ocean dynamic processes are introduced. Figure 16 demonstrates four horizontal oceanic advection terms in the upper-ocean heat budget. From the heat budget aspect, we observe the artificial warming during post-El Niño summers due to two oceanic zonal advection terms in CMIP models. First, the excessive westward extension of simulated El Niño-related positive SSTA can enhance the horizontal SSTA gradient ( $-\partial T'/\partial x$ ) over the equatorial WP. Thus, the mean-state zonal warm advection ( $-\bar{u}\partial T'/\partial x$ ) will bring about a more westward-extended El Niño-related warming

pattern in CMIP models (Fig. 16b, c). Second, the mean-state horizontal SST gradient ( $-\partial \bar{T}/\partial x$ ) over the equatorial WP is enhanced possibly due to the cold tongue bias in CMIP models. Therefore, the anomalous eastward ocean current on the equator could lead to a stronger anomalous zonal warm advection ( $-u'\partial \bar{T}/\partial x$ ), favoring SST warming over the equatorial WP and forming zonal advection feedback during post-El Niño summers (Fig. 16h, i). Besides, we also observe a notable equatorial Pacific warming bias induced by the mean meridional advection of anomalous temperature gradient ( $-\bar{v}\partial T'/\partial y$ ) during post-El Niño summers (Fig. 16e, f). The meridional SSTA gradient ( $-\partial T'/\partial y$ ) over the equatorial WP may be related with westward-extended positive SSTA as well. The contributions from the anomalous meridional advection of mean temperature gradient ( $-v'\partial \bar{T}/\partial y$ ) are relatively small (Fig. 16k, l). Similar conclusions can be obtained via the regression analysis (Supplementary Fig. S12). In addition, previous studies suggested that the contribution of mean vertical advection of anomalous potential temperature gradient ( $-\bar{w}\partial T'/\partial z$ ), known as thermocline feedback, is also of vital importance during the post-El Niño summer (Kug et al. 2010; Chen and Li 2021). Therefore, we further investigate the potential contributions of thermocline feedback ( $-\bar{w}\partial T'/\partial z$ ) and upwelling feedback ( $-\omega'\partial \bar{T}/\partial z$ ) to equatorial WP warming bias (Fig. 17). The thermocline feedback and upwelling feedback are generally well captured in CMIP6 models and may not be the main causes for the long-lasting WP warming bias.

From the oceanic fluctuation view, the westerly wind bias emerges on the equatorial WP during post-El Niño summer in CMIP models (Fig. 13d, e), which may be related to the weak persistence of simulated summer AAC. This westerly wind bias could trigger the downwelling ocean Kelvin waves that propagate eastward and help maintain the El Niño. The artificial persistence of El Niño in the simulations (Fig. 4) can lead to the equatorial WP warming bias, which may in turn undermine the AAC persistence and form wind–downwelling–SST feedback.

## 5 Discussion

In this section, we further examine the persistence of AAC during post-EP and post-CP El Niño summers. All the three criteria have the ability to distinguish two types of El Niño during El Niño developing winter (Supplementary Figs. S13, S14, S15). Figure 18 illustrates the composite monthly 850-hPa wind and precipitation anomalies during post-EP and post-CP El Niño summers (identified with Niño-3 and Niño-4 index) in the observations, CMIP5 and CMIP6 MME. The observational AAC and rainfall anomalies during post-EP El Niño summers bear notable similarities with

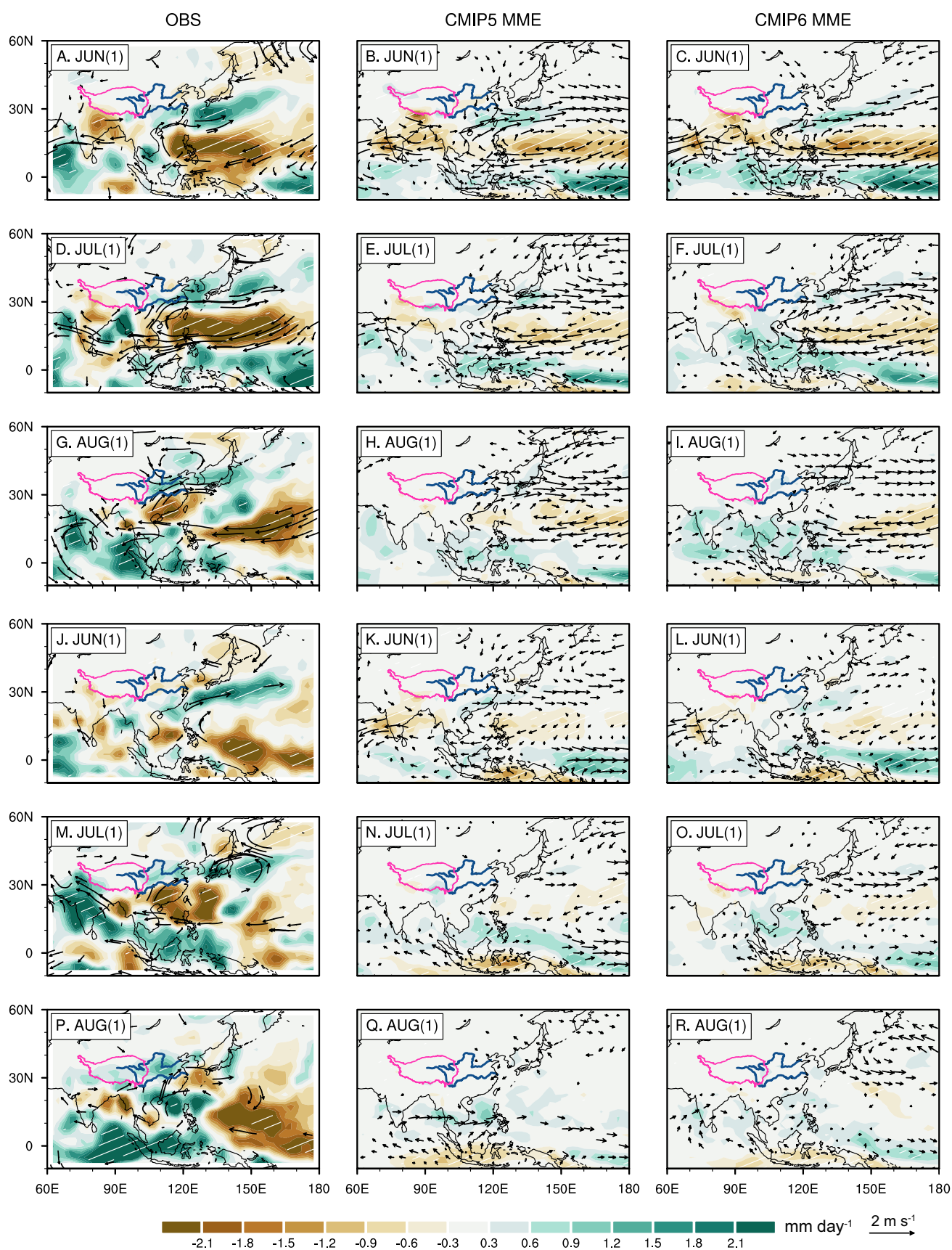


**Fig. 18** 850-hPa wind (vectors; units:  $\text{m s}^{-1}$ ) and precipitation (colors; units:  $\text{mm day}^{-1}$ ) anomalies for the EP (A–I) and CP (J–R) El Niño composite (identified with Niño-3 and Niño-4 index) in the observations (left panels), CMIP5 MME (middle panels), and CMIP6 MME (right panels) during post-El Niño summers. Vectors only exceeding the 95% confidence level are shown. White hatchings denote that the anomalies are significant at the 95% confidence level (for observations) or more than 80% of models agree with the sign of the MME (for CMIP models)

those during entire post-El Niño summers (Fig. 18a, d, g). Besides, we find a slight improved simulation skill of AAC persistence during post-EP El Niño late summer compared with the entire post-El Niño late summer in CMIP models (Fig. 18h, i). The composite results during post-CP El Niño summers differ from those in post-EP El Niño summers. Specifically, the observational AAC and precipitation anomalies are weak and loosely organized during post-CP El Niño summers (Fig. 18j, m, p), consistent with previous study (Feng et al. 2011). In CMIP models, the simulated AAC and precipitation anomalies are weak and almost insignificant during post-CP El Niño late summers (Fig. 18n, o, q, r). Similar conclusions could be drawn from the other two classification methods (Supplementary Figs. S17 and S19) and extended time periods (Supplementary Figs. S16, S18 and S20). To get insight into the mechanisms of AAC patterns during post-EP and post-CP El Niño summers, the composite SSTA patterns are further shown (Supplementary Figs. S21, S22 and S23). The simulated NIO–WP SSTA gradients during post-EP El Niño summers are generally consistent with those during the entire post-El Niño summers in CMIP models. However, the WP warming bias is too westward-extended in CMIP models during post-CP El Niño summers. As a result, the simulated NIO–WP SSTA gradients could barely persist, which may lead to the disappearance of AAC during post-CP El Niño late summer.

The weak persistence bias of summertime AAC will inevitably lead to an overall underestimation of summer seasonal mean AAC. Thus, future studies should be careful when evaluating and projecting El Niño-related summer AAC and coherent climate impacts in CMIP5 and CMIP6 models. We recommend that models with relatively high simulation skills should be selected first rather than simply using all available model simulations. Here, we use the monthly AAC index to preliminarily identify the most skillful CMIP models. Future studies could use more comprehensive metrics to select high-skill models based on their particular applications or societal needs. In this section, if the AAC indices of a single model in June(1), July(1) and August(1) surpass 1 simultaneously, it will be deemed as the high-performance model. Slight varying thresholds (0.8 and 1.2) will not change the composite results. Three CMIP5 models (CESM1-WACCM, GFDL-CM3, NorESM1-ME) and eight CMIP6 models (CESM2-FV2, CESM2-WACCM-FV2,

CESM2, E3SM-1-1-ECA, E3SM-1-1, GISS-E2-1-H, KACE-1-0-G, MIROC-ES2L) are selected based on this criterion. The selected optimal model set MME performs significantly better than the whole CMIP5/6 ensemble. The general characteristics of the observed AAC and precipitation anomalies in August(1) can be well captured (Fig. 19h, i). Correspondingly, the IOB warming strongly maintains while WP warming bias dissipates during post-El Niño late summer in the high-performance CMIP5 and CMIP6 MME (Fig. 20h, i). In addition, we observe a more realistic simulation of mean-state SWIO thermocline dome and equatorial Pacific cold tongue in the high-performance CMIP5 and CMIP6 MME than their raw counterparts (Supplementary Figs. S24 and S25). This mean-state simulation improvement may contribute to the generally good persistence of the NIO–WP SSTA gradient in high-performance models (Fig. 20).

## 6 Summary

The present study provides a systematical investigation of weak persistence of AAC during post-El Niño summers and unveils its possible physical mechanisms based on 45 CMIP6 and 36 CMIP5 models. In contrast with the observational sub-seasonal intensification, the simulated AAC fails to persist through post-El Niño summers in the CMIP5 and CMIP6 MME. Here, we suggest that the weak persistence of NIO–WP SSTA gradient rooted in the poorly represented climate background mean-states may be responsible for biased persistence of AAC during post-El Niño summers (Fig. 21). On one hand, the IOB warming decays faster in CMIP5 and CMIP6 MME compared with the observations during post-El Niño summers. Upper-ocean heat budget diagnoses indicate that the weak persistence of anomalous latent heat flux and shortwave radiation should be largely responsible for that of the IOB warming. The simulated thermocline dome in SWIO is much deeper in CMIP5 and CMIP6 MME compared with the observation. It may lead to weaker oceanic Rossby wave-induced thermocline feedback and weakened cross-equatorial C-shaped wind patterns during post-El Niño spring and early summer. The weakened northeasterly wind anomalies over NIO cause the dampened WES feedback and reduced latent heating anomalies, finally resulting in the weak persistence of IOB warming. The weak persistence of inter-basin positive feedback between IOB warming and AAC pattern also plays a major role. On the other hand, the WP warming bias persists throughout post-El Niño summer in CMIP5 and CMIP6 MME and ocean dynamic processes play an important role in this case. Specifically, the simulated mean-state cold tongue in the WP is colder and more westward-extended in CMIP5

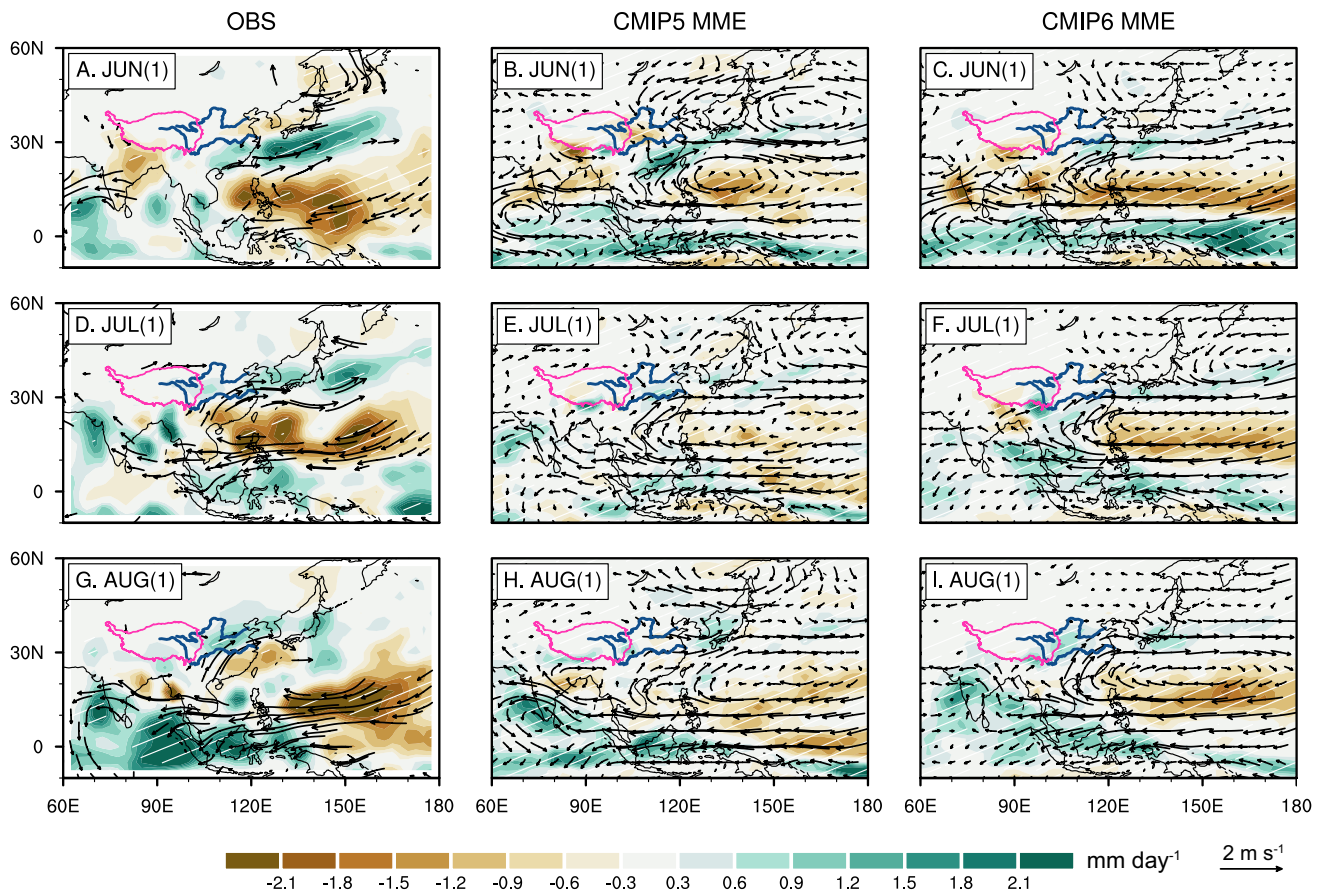


**Fig. 19** Same as Fig. 1, but for 850-hPa wind (vectors; units:  $\text{m s}^{-1}$ ) and precipitation (colors; units:  $\text{mm day}^{-1}$ ) anomalies in high-performance models

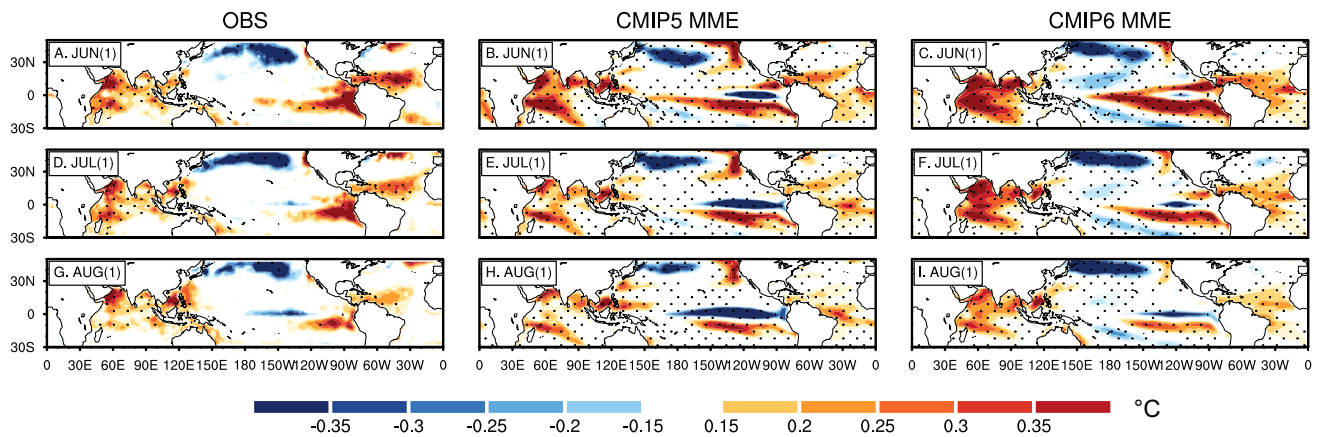


**Fig. 20** Same as Fig. 4, but for SSTA (colors; units:  $^{\circ}\text{C}$ ) in high-performance models

and CMIP6 MME than in the observation, resulting in the intensified upper-ocean zonal advection feedback and wind–downwelling–SST feedback, thereby favoring the persistence of WP warming bias throughout post-El Niño summers. This long-lasting unrealistic WP warming bias

may excite westward spreading Rossby wave and attenuate NIO warming-induced eastward propagating Kelvin wave, finally leading to the weak persistence of AAC. Apart from the NIO–WP SSTA gradient, the weakened background NWP summer monsoon onset in CMIP models

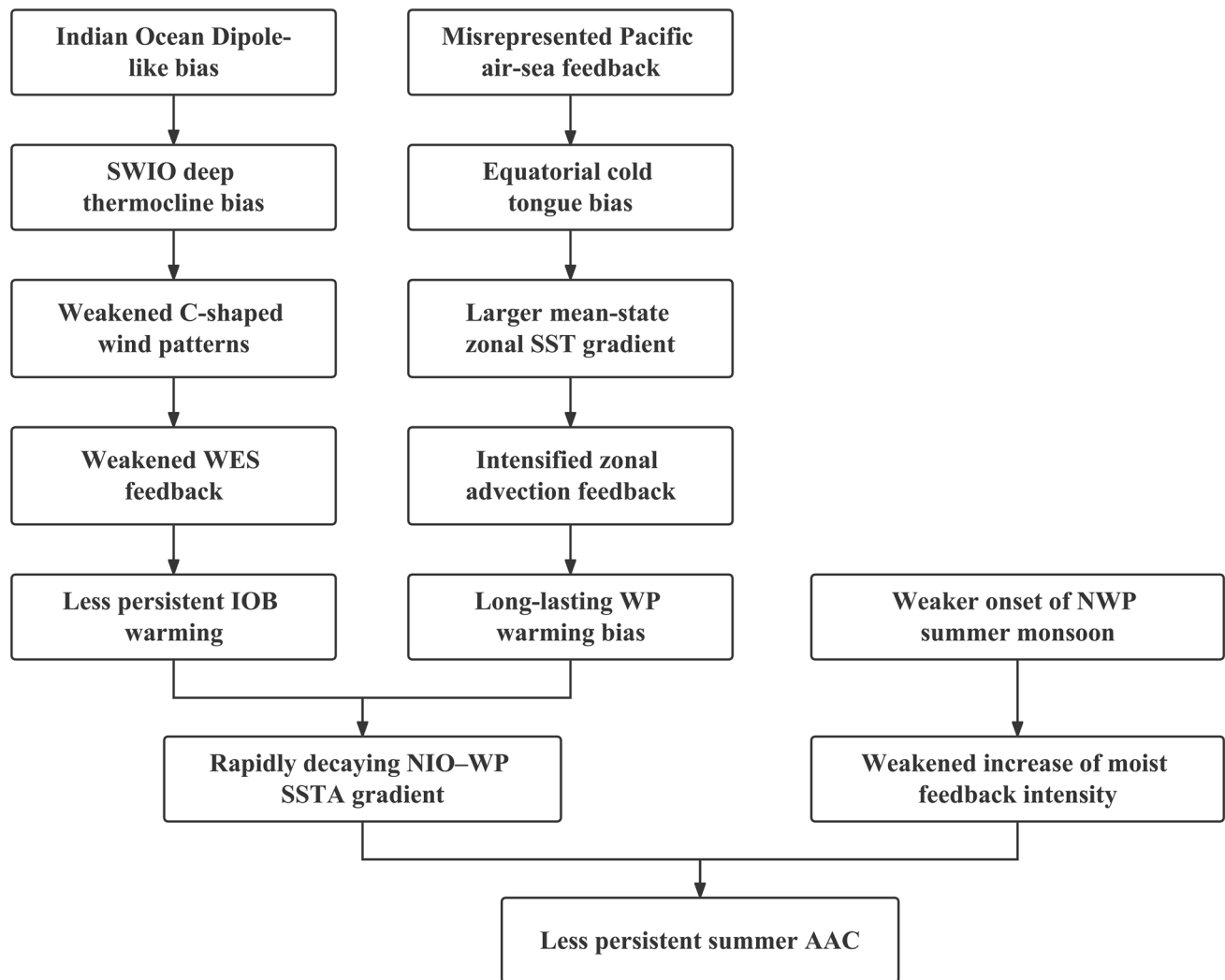


**Fig. 21** Schematic diagram depicting mechanisms of weak persistence of AAC during post-El Niño summers in CMIP5 and CMIP6 models

may suppress increase of moist/convection–circulation feedback intensity in August(1), which may result in the weakened summertime AAC intensification compared with the observation.

Previous studies suggested that SWIO deep thermocline bias may stem from IO Dipole-like bias (Li et al. 2015; Zheng et al. 2016) while the equatorial cold tongue bias may originate from the misrepresented ocean–atmosphere feedback in the Pacific in CMIP models (Li and Xie 2014). Compared with CMIP5 models, CMIP6 models simulate a more realistic SWIO thermocline dome and equatorial Pacific cold tongue, though evidence for the latter is less robust. As a result, CMIP6 models could simulate a more realistic AAC persistence than their CMIP5 counterparts. The weak persistence bias of summer AAC may potentially restrict the models’ prediction and projection skills in the Asian monsoon during late summer. Therefore, the present study highlights the significance of a more realistic simulation of

mean-state SWIO thermocline dome and equatorial Pacific cold tongue to better reproduce the persistence of summer AAC and its climate impacts in CGCMs.

It is noteworthy that the AAC could result in positive SSTA in the NWP and south China sea (Fig. 4a, d, g), which will strengthen the local deep convection and decrease the downward shortwave radiation, thereby damping the AAC and forming the negative cloud–radiation–SST feedback. Thus, local positive SSTA and WP warming bias tend to dissipate the AAC pattern, whereas the NIO warming maintains the AAC during post-El Niño summers. In August(1), the damping effects outweigh the IO capacitor effect in CMIP models, leading to the rapid decay of AAC over the EA–NWP. In addition to SSTA pattern impacts, the anomalous subtropical Meiyu/Baiu rainfall serving as the heat source may also be vital in anchoring the AAC pattern (Lu and Lin 2009). In the observational August(1), the AAC induces and is in turn geographically fixed by the anomalous

rainband in its northern flank (Fig. 1g). However, the AAC displaces eastward and disappears over EA in August(1) in CMIP5 and CMIP6 MME (Fig. 1h, i), resulting in the vanishment of anomalous rainband. Without the positive feedback from this subtropical rainfall-induced heating anomaly, the AAC is more loosely organized and far away from the mainland in CMIP models. Previous researches have suggested that NIO SSTA depend largely on the simulated ENSO in the Pacific via the atmospheric bridge (Klein et al. 1999; Alexander et al. 2002). Whether the weak persistence of IOB warming interacts with long-lasting WP warming bias is intriguing and entails future study.

**Supplementary Information** The online version contains supplementary material available at <https://doi.org/10.1007/s00382-023-06772-0>.

**Acknowledgements** We would like to thank two anonymous reviewers for their insightful and constructive comments that significantly improve the quality of the manuscript. We also acknowledge the World Climate Research Programme's Working Group on Coupled Modelling, and we thank the climate modeling groups across the world (listed in Table 1) for producing and making publicly available their model outputs.

**Author contributions** HT, KH, and GH conceived the study, designed the methodology and built the mechanisms. HT performed the formal analyses and wrote the draft manuscript. GH, KH, WJ, WT, YW and HH contributed to improving the manuscript and assisted in the interpretation of the results.

**Funding** This work is supported by the National Basic Research Program of China (2019YFA0606703), the Strategic Priority Research Program of Chinese Academy of Sciences (XDA20060500), the National Natural Science Foundation of China (42175040, 41831175, 41661144016, 42141019, 91937302, 41721004), Key Deployment Project of Centre for Ocean Mega-Research of Science, Chinese Academy of Sciences (COMS2019Q03). The work was also supported by the Chinese Jiangsu Collaborative Innovation Center for Climate Change and the Youth Innovation Promotion Association of CAS (2021072).

**Data availability** All the data that support the findings are available for open access. The CMAP precipitation data is located at <https://psl.noaa.gov/data/gridded/data.cmap.html>. The CMIP5/6 model outputs can be accessed at the ESGF portal (<https://esgf-node.llnl.gov/projects/esgf-llnl/>). The NCEP–NCAR atmospheric reanalysis is located at <https://psl.noaa.gov/data/gridded/data.ncep.reanalysis.html>. HadISST dataset could be accessed from <https://www.metoffice.gov.uk/hadobs/hadist/>. SODA datasets could be accessed from [http://www2.atmos.umd.edu/~ocean/index\\_files/](http://www2.atmos.umd.edu/~ocean/index_files/). All the codes for analyses and diagnostics are available from the corresponding authors upon reasonable request.

## Declarations

**Conflict of interest** The authors have no competing interests as defined by Springer, or other interests that might be perceived to influence the results and/or discussion reported in this paper.

## References

- Alexander MA, Blade I, Newman M, Lanzante JR, Lau N-C, Scott JD (2002) The atmospheric bridge: the influence of ENSO teleconnections on air–sea interaction over the global oceans. *J Clim* 15:2205–2231
- Ashok K, Behera SK, Rao SA, Weng H, Yamagata T (2007) El Niño Modoki and its possible teleconnection. *J Geophys Res Oceans* 112:1–27
- Carton JA, Giese BS (2008) A reanalysis of ocean climate using simple ocean data assimilation (SODA). *Mon Weather Rev* 136:2999–3017
- Chang CP, Zhang Y, Li T (2000) Interannual and interdecadal variations of the East Asian summer Monsoon and tropical Pacific SSTs. Part I: roles of the subtropical ridge. *J Clim* 13(24):4310–4325
- Chen M, Li T (2021) ENSO evolution asymmetry: EP versus CP El Niño. *Clim Dyn* 56(11):3569–3579
- Chen M, Li T, Shen X, Wu B (2016) Relative roles of dynamic and thermodynamic processes in causing evolution asymmetry between El Niño and La Niña. *J Clim* 29:2201–2220
- Chowdary JS, Xie S-P, Lee J-Y, Kosaka Y, Wang B (2010) Predictability of summer northwest Pacific climate in 11 coupled model hindcasts: local and remote forcing. *J Geophys Res Atmos* 115:1–16
- Chowdary JS, Gnanaseelan C, Chakravorty S (2013) Impact of North-west Pacific anticyclone on the Indian summer monsoon region. *Theor Appl Climatol* 113:329–336
- Deng K, Yang S, Ting M, Zhao P, Wang Z (2019) Dominant modes of China summer heat waves driven by global sea surface temperature and atmospheric internal variability. *J Clim* 32:3761–3775
- Du Y, Xie SP, Huang G, Hu K (2009) Role of air–sea interaction in the long persistence of El Niño-induced north Indian Ocean warming. *J Clim* 22(8):2023–2038
- Du Y, Yang L, Xie SP (2011) Tropical Indian ocean influence on northwest Pacific Tropical cyclones in summer following strong El Niño. *J Clim* 24(1):315–322
- Du Y, Xie S-P, Yang Y-L, Zheng X-T, Liu L, Huang G (2013) Indian Ocean variability in the CMIP5 multimodel ensemble: the basin mode. *J Clim* 26(18):7240–7266
- Du Y, Chen Z, Xie S-P, Zhang L, Zhang Y, Cai Y (2022) Drivers and characteristics of the Indo-western Pacific Ocean capacitor. *Front Clim* 4:1014138
- Eyring V, Bony S, Meehl GA, Senior CA, Stevens B, Stoufer RJ, Taylor KE (2016) Overview of the Coupled Model Intercomparison Project Phase 6 (CMIP6) experimental design and organization. *Geosci Model Dev* 9(5):1937–1958
- Feng J, Chen W, Tam CY, Zhou W (2011) Different impacts of El Niño and El Niño Modoki on China rainfall in the decaying phases. *Int J Climatol* 31:2091–2101
- Freund MB, Brown JR, Henley BJ, Karoly DJ, Brown JN (2020) Warming patterns affect El Niño diversity in CMIP5 and CMIP6 models. *J Clim* 33(19):8237–8260
- Gill AE (1980) Some simple solutions for heat-induced tropical circulation. *Q J R Meteorol Soc* 106:447–462
- Grose MR, Narsey S, Delage FP et al (2020) Insights from CMIP6 for Australia's future climate. *Earth's Future* 8:e2019EF001469
- He C, Zhou T (2015) Responses of the Western North Pacific subtropical high to global warming under RCP4.5 and RCP8.5 scenarios projected by 33 CMIP5 models: the dominance of tropical Indian Ocean–tropical Western Pacific SST gradient. *J Clim* 28:365–380
- Hou M, Tang Y (2022) Recent progress in simulating two types of ENSO—from CMIP5 to CMIP6. *Front Mar Sci* 9:986780

- Hu K, Huang G, Huang R (2011) The impact of tropical Indian Ocean variability on summer surface air temperature in China. *J Clim* 24(20):5365–5377
- Hu K, Huang G, Zheng X-T, Xie S-P, Qu X, Du Y, Liu L (2014) Interdecadal variations in ENSO influences on Northwest Pacific-East Asian early summertime climate simulated in CMIP5 models. *J Clim* 27(15):5982–5998
- Hu K, Huang G, Xie S-P, Long S-M (2019) Effect of the mean flow on the anomalous anticyclone over the Indo-Northwest Pacific in post-El Niño summers. *Clim Dyn* 53(9–10):5725–5741
- Hu K, Huang G, Huang P, Kosaka Y, Xie S-P (2021) Intensification of El Niño-induced atmospheric anomalies under greenhouse warming. *Nat Geosci* 14:377–382
- Huang RH, Sun FY (1992) Impacts of the tropical western Pacific on the East-Asian summer monsoon. *J Meteorol Soc Jpn* 70(1B):243–256
- Jiang Z, Li J (2022) Impact of eastern and central Pacific El Niño on lower tropospheric ozone in China. *Atmos Chem Phys* 22(11):7273–7285
- Jiang W, Huang G, Hu K, Wu R, Gong H, Chen XL, Tao W (2017) Diverse relationship between ENSO and the northwest Pacific summer climate among CMIP5 models: dependence on the ENSO decay pace. *J Clim* 30:109–127
- Jiang W, Huang G, Huang P, Wu R, Hu K, Chen W (2019) Northwest Pacific anticyclonic anomalies during Post-El Niño summers determined by the pace of El Niño Decay. *J Clim* 32:3487–3503
- Jiang W, Huang P, Huang G, Ying J (2021) Origins of the excessive westward extension of ENSO SST simulated in CMIP5 and CMIP6 models. *J Clim* 34(8):2839–2851
- Jiang W, Gong H, Huang P, Wang L, Huang G, Hu L (2022) Biases and improvements of the ENSO-East Asian winter monsoon teleconnection in CMIP5 and CMIP6 models. *Clim Dyn* 59:2467–2480
- Kalnay E, Kanamitsu M, Kistler R, Collins W, Deaven D, Gandin L, Iredell M, Saha S, White G, Woollen J, Zhu Y, Chelliah M, Ebisuzaki W, Higgins W, Janowiak J, Mo KC, Ropelewski C, Wang J, Leetmaa A, Reynolds R, Jenne R, Joseph D (1996) The NCEP/NCAR 40-year reanalysis project. *Bull Am Meteorol Soc* 77(3):437–471
- Kim H-M, Webster PJ, Curry JA, Toma VE (2012) Asian summer monsoon prediction in ECMWF System 4 and NCEP CFSv2 retrospective seasonal forecasts. *Clim Dyn* 39:2975–2991
- Klein SA, Soden BJ, Lau N-C (1999) Remote sea surface temperature variations during ENSO: evidence for a tropical atmospheric bridge. *J Clim* 12:917–932
- Kosaka Y, Xie S-P, Lau NC, Vecchi GA (2013) Origin of seasonal predictability for summer climate over the Northwestern Pacific. *Proc Natl Acad Sci* 110(19):7574–7579
- Kug JS, Choi J, An SI, Jin FF, Wittenberg AT (2010) Warm pool and cold tongue El Niño events as simulated by the GFDL 2.1 coupled GCM. *J Clim* 23(5):1226–1239
- Lee T, Waliser DE, Li J-L, Landerer FW, Gierach MM (2013) Evaluation of CMIP3 and CMIP5 wind stress climatology using satellite measurements and atmospheric reanalysis products. *J Clim* 26(16):5810–5826
- Li G, Xie S-P (2014) Tropical biases in CMIP5 multimodel ensemble: the excessive equatorial Pacific cold tongue and double ITCZ problems. *J Clim* 27:1765–1980
- Li G, Xie S-P, Du Y (2015) Climate model errors over the South Indian Ocean thermocline dome and their effect on the basin mode of interannual variability. *J Clim* 28:3093–3098
- Li T, Wang B, Wu B, Zhou TJ, Chang CP, Zhang RH (2017) Theories on formation of an anomalous anticyclone in western North Pacific during El Niño: a review. *J Meteorol Res* 31:987–1006
- Li G, Jian Y, Yang S, Du Y, Wang Z, Li Z, Zhuang W, Jiang W, Huang G (2019) Effect of excessive equatorial Pacific cold tongue bias on the El Niño-Northwest Pacific summer monsoon relationship in CMIP5 multi-model ensemble. *Clim Dyn* 52(9–10):6195–6212
- Li S, Gong Z, Zhang S, Yang J, Qiao S, Feng G (2022) Decadal variation of the precipitation relationship between June and August over South China and its mechanism. *Clim Dyn* 59:1863–1882
- Lu R, Lin Z (2009) Role of subtropical precipitation anomalies in maintaining the summertime meridional teleconnection over the Western North Pacific and East Asia. *J Clim* 22:2058–2072
- Matsuno T (1966) Quasi-geostrophic motions in the equatorial area. *J Meteorol Soc Jpn* 44:25–43
- McPhaden MJ, Zebiak SE, Glantz MH (2006) ENSO as an integrating concept in Earth science. *Science* 314:1740–1745
- Nitta T (1987) Convective activities in the tropical western Pacific and their impact on the northern hemisphere summer circulation. *J Meteorol Soc Jpn* 65:165–171
- Ohba M, Ueda H (2006) A role of zonal gradient of SST between the Indian Ocean and the Western Pacific in localized convection around the Philippines. *SOLA* 2:176–179
- Planton YY, Guilyardi E, Wittenberg AT, Lee J, Gleckler PJ, Bayr T, McGregor S, McPhaden MJ, Power S, Roehrig R, Vialard J, Voldoire A (2021) Evaluating climate models with the CLIVAR 2020 ENSO metrics package. *Bull Am Meteorol Soc* 102(2):E193–E217
- Rayner NA, Parker DE, Horton EB, Folland CK, Alexander LV, Rowell DP, Kent EC, Kaplan A (2003) Global analyses of sea surface temperature, sea ice, and night marine air temperature since the late nineteenth century. *J Geophys Res Atmos* 108(D14):4407
- Ren HL, Jin FF (2011) Niño indices for two types of ENSO. *Geophys Res Lett* 38:L04704
- Takaya K, Nakamura H (2001) A formulation of a phase-independent wave-activity flux for stationary and migratory quasi-geostrophic eddies on a Zonally Varying Basic Flow. *J Atmos Sci* 58(6):608–627
- Tang HS, Hu KM, Huang G, Wang Y, Tao W (2021) Intensification and Northward extension of Northwest Pacific anomalous anticyclone in El Niño decaying mid-summer: an energetic perspective. *Clim Dyn* 58:591–606
- Tang H, Wang Z, Tang B, Ma Y, Pei L, Tian F, Wang J, Nanding N, Sparrow S, Tett S, Dong B, Lott F (2022a) Reduced probability of 2020 June–July persistent heavy Meiyu rainfall event in the mid-lower reaches of the Yangtze River basin under anthropogenic forcing. *Bull Am Meteorol Soc* 103(3):S83–S89
- Tang HS, Wang J, Hu KM, Huang G, Chowdary JS, Wang Y, Wang Z, Tang B (2022b) Increasing 2020-like boreal summer rainfall extremes over Northeast Indian subcontinent under greenhouse warming. *Geophys Res Lett* 49(11):e2021GL096377
- Tao W, Huang G, Hu K, Gong H, Wen G, Liu L (2016) A study of biases in simulation of the Indian Ocean basin mode and its capacitor effect in CMIP3/CMIP5 models. *Clim Dyn* 46:205–226
- Tao W, Huang G, Wu R, Hu K, Wang P, Gong H (2018) Origins of biases in CMIP5 Models simulating Northwest Pacific summertime atmospheric circulation anomalies during the decaying phase of ENSO. *J Clim* 31(14):5707–5729
- Tao W, Wang P, Liu Y, Wen G, Dong D (2019) Dominant modes of CMIP3/5 models simulating northwest Pacific circulation anomalies during post-ENSO summer and their SST dependence. *Theor Appl Climatol* 138:1809–1820
- Tao SY, Chen LX (1987) A review of recent research on the East Asian summer monsoon in China. In: Chang CP, Krishnamurti TN (eds) *Monsoon meteorology*. Oxford University Press, New York

- Taylor KE, Stouffer RJ, Meehl GA (2012) An overview of CMIP5 and the experiment design. *Bull Am Meteorol Soc* 93(4):485–498
- Wang B, Fan Z (1999) Choice of South Asian summer monsoon indices. *Bull Amer Meteor Soc* 80:629–638
- Wang B, Wu R, Fu X (2000) Pacific-East Asian Teleconnection: How Does ENSO Affect East Asian Climate? *J Clim* 13(9):1517–1536
- Wang X, Li T, He C (2021) Impact of the mean state on El Niño induced western North Pacific anomalous anticyclone during its decaying summer in AMIP models. *J Clim* 34(22):1–49
- Wu RG, Kirtman BP, Krishnamurthy V (2008) An asymmetric mode of tropical Indian Ocean rainfall variability in boreal spring. *J Geophys Res Atmos* 113:D05104
- Wu B, Zhou TJ, Li T (2009) Seasonally evolving dominant interannual variability modes of East Asian climate. *J Clim* 22(11):2992–3005
- Wu B, Li T, Zhou TJ (2010) Relative contributions of the Indian Ocean and local SST anomalies to the maintenance of the western North Pacific anomalous anticyclone during the El Niño decaying summer. *J Clim* 23(11):2974–2986
- Xiang B, Wang B, Yu W, Xu S (2013) How can anomalous western North Pacific Subtropical High intensify in late summer? *Geophys Res Lett* 40(10):2349–2354
- Xie P, Arkin PA (1997) Global precipitation: a 17-year monthly analysis based on gauge observations, satellite estimates. *Bull Am Meteorol Soc* 78(11):2539–2558
- Xie SP, Annamalai H, Schott F, McCreary JP (2002) Structure and mechanisms of south Indian Ocean climate variability. *J Clim* 15:864–878
- Xie S-P, Hu K, Hafner J, Tokinaga H, Du Y, Huang G, Sampe T (2009) Indian Ocean Capacitor Effect on Indo-Western Pacific Climate during the Summer following El Niño. *J Clim* 22(3):730–747
- Xie S-P, Deser C, Vecchi GA, Ma J, Teng H, Wittenberg AT (2010) Global warming pattern formation: sea surface temperature and rainfall. *J Clim* 23(4):966–986
- Xie S-P, Kosaka Y, Du Y, Hu K, Chowdary JS, Huang G (2016) Indo-western Pacific Ocean capacitor and coherent climate anomalies in post-ENSO summer: a review. *Adv Atmos Sci* 33(4):411–432
- Xu K, Tam CY, Zhu C, Liu B, Wang W (2017) CMIP5 projections of two types of El Niño and their related tropical precipitation in the twenty-first century. *J Clim* 30(3):849–864
- Yang X, Huang P (2022) Improvements in the relationship between tropical precipitation and sea surface temperature from CMIP5 to CMIP6. *Clim Dyn*. <https://doi.org/10.1007/s00382-022-06519-3>
- Ye H, Lu R (2010) Subseasonal variation in ENSO-related East Asian Rainfall Anomalies during summer and its role in weakening the relationship between the ENSO and summer Rainfall in Eastern China since the Late 1970s. *J Clim* 24(9):2271–2284
- Yeh SW, Kug JS, Dewitte B, Kwon MH, Kirtman BP, Jin FF (2009) El Niño in a changing climate. *Nature* 461:511–514
- Yu JY, Kim ST (2013) Identifying the types of major El Niño events since 1870. *Int J Climatol* 33(8):2105–2112
- Yu JY, Zou Y, Kim ST, Lee T (2012) The changing impact of El Niño on US winter temperatures. *Geophys Res Lett* 39(15):L15702
- Yu T, Feng J, Chen W, Wang X (2021) Persistence and breakdown of the western North Pacific anomalous anticyclone during the EP and CP El Niño decaying spring. *Climate Dyn* 57:3529–3544
- Yuan Y, Yang S (2012) Impacts of different types of El Niño on the East Asian climate: Focus on ENSO cycles. *J Clim* 25:7702–7722
- Zheng X-T, Gao L, Li G, Du Y (2016) The southwest Indian Ocean thermocline dome in CMIP5 models: historical simulation and future projection. *Adv Atmos Sci* 33:489–503
- Zou Y, Yu JY, Lee T, Lu MM, Kim ST (2014) CMIP5 model simulations of the impacts of the two types of El Niño on the US winter temperature. *J Geophys Res Atmos* 119(6):3076–3092

**Publisher's Note** Springer Nature remains neutral with regard to jurisdictional claims in published maps and institutional affiliations.

Springer Nature or its licensor (e.g. a society or other partner) holds exclusive rights to this article under a publishing agreement with the author(s) or other rightsholder(s); author self-archiving of the accepted manuscript version of this article is solely governed by the terms of such publishing agreement and applicable law.